

Vertical Profiles of the Wave-Induced Airflow above Ocean Surface Waves

LAURENT GRARE, LUC LENAIN, AND W. KENDALL MELVILLE

Scripps Institution of Oceanography, La Jolla, California

(Manuscript received 14 June 2018, in final form 4 October 2018)

ABSTRACT

An analysis of coherent measurements of winds and waves from data collected during the ONR Southern California 2013 (SoCal2013) program from R/P *FLIP* off the coast of Southern California in November 2013 is presented. An array of ultrasonic anemometers mounted on a telescopic mast was deployed to resolve the vertical profile of the modulation of the marine atmospheric boundary layer by the waves. Spectral analysis of the data provides the wave-induced components of the wind velocity for various wind-wave conditions. Results show that the wave-induced fluctuations depend both on the spectral wave age $c(\omega)/U(z)$ and the normalized height kz , where c is the linear phase speed of the waves with wavenumber k and $U(z)$ is the mean wind speed measured at the height z . The dependence on the spectral wave age expresses the sensitivity of the wave-induced airflow to the critical layer where $U(z) = c$. Across the critical layer, there is a significant change of both the amplitude and phase of the wave-induced fluctuations. Below the critical layer, the phase remains constant while the amplitude decays exponentially depending on the normalized height. Accounting for this double dependency, the nondimensionalization of the amplitude of the wave-induced fluctuations by the surface orbital velocity akc collapses all the data measured by the array of sonic anemometers, where a is the amplitude of the waves.


1. Introduction


The interactions between turbulent winds and ocean waves play essential roles in many important atmosphere–ocean phenomena. They drive the exchange of mass, momentum, and heat between the atmosphere and the ocean, which are key processes needed to validate and improve models of the atmosphere, the upper ocean, and the waves. To understand and parameterize the processes occurring at, above, and below the wavy sea surface, an explicit description of the airflow over surface waves is needed to improve our knowledge of air–sea fluxes for weather and climate predictions.

The problem of flow over surface waves has been an active research topic for almost a century. Many theoretical studies (Jeffreys 1925; Phillips 1957; Miles 1957,

1993; Janssen 1991; Belcher and Hunt 1993; among others) have focused on explaining the mechanism of wind-wave generation and growth. Meanwhile, the quantification of wind-wave energy and momentum transfer and wavefield evolution has relied substantially on field (e.g., Dobson 1971; Elliott 1972; Snyder et al. 1981; Hristov et al. 2003; Donelan et al. 2006; Grare et al. 2013a; Hogstrom et al. 2015) and laboratory measurements (e.g., Hsu and Hsu 1983; Banner and Peirson 1998; Veron et al. 2007; Grare et al. 2013b; Buckley and Veron 2016).

In addition to theoretical and experimental studies, numerical simulations of turbulent winds over waves have greatly contributed to our understanding of these phenomena. Early studies focused on solving the Reynolds-averaged Navier–Stokes (RANS) equations (Townsend 1972; Gent and Taylor 1976; Al-Zanaidi and Hui 1984; Van Duin and Janssen 1992; Mastenbroek et al. 1996). The growth of computing power has made direct numerical simulation (DNS) possible for the study of turbulent winds over waves under idealized conditions (Sullivan et al. 2000; Kihara et al. 2007; Yang and Shen 2009, 2010). More recently, large-eddy simulation (LES) has become a common approach for the study of winds over ocean waves (Sullivan et al. 2008, 2014; Liu et al. 2010; Yang et al. 2013; Wu et al. 2017).

 Denotes content that is immediately available upon publication as open access.

 Supplemental information related to this paper is available at the Journals Online website: <https://doi.org/10.1175/JPO-D-18-0121.s1>.

Corresponding author: Laurent Grare, lgrare@ucsd.edu

DOI: 10.1175/JPO-D-18-0121.1

© 2018 American Meteorological Society. For information regarding reuse of this content and general copyright information, consult the [AMS Copyright Policy](#) (www.ametsoc.org/PUBSReuseLicenses).

Recently, there has been a growing interest in waves traveling faster than the wind (often referred to as the regime of “wave-driven wind”) as Hanley et al. (2010) have shown that the wind and the waves are often not in equilibrium; that is, local wave conditions are not necessarily tied to the local wind conditions. That is, the wave-driven wind regime is a common feature around the globe. Sullivan et al. (2008), Hogstrom et al. (2009), Smedman et al. (2009), Soloviev and Kudryavtsev (2010), Hogstrom et al. (2015), and Wu et al. (2017) have focused on this wave-driven regime showing the existence of an upward transfer of momentum from the swell to the wind, leading sometimes to the presence of a jet in the lower part of the marine atmospheric boundary layer (MABL). In this regime, the amplitude of the wave-induced fluctuations of the wind components can compare with the amplitude of the background turbulence, playing a nonnegligible role in the production of turbulence, driving the exchange of momentum between the atmosphere and the ocean, and affecting the shape of the vertical profile of the mean wind speed (Hristov and Ruiz-Plancarte 2014). While the recent developments of LES are able to phase-resolve the airflow above 3D wave fields (Sullivan et al. 2014) and offer further promise to better understand the physics of the air–sea interaction, experimental data remain the ultimate test of these numerical simulations to describe real flows.

In the present paper, we present results from a field experiment showing that the wave-induced fluctuations depend both on the spectral wave age $c(\omega)/U(z)$ and the normalized height kz above the mean sea surface. The dependence on the spectral wave age expresses the sensitivity of the wave-induced airflow to the critical layer, while the dependence on the normalized height expresses the vertical decay of the wave-induced fluctuations in the air above the waves. We show that the nondimensionalization of the amplitude of the wave-induced fluctuations by the surface orbital velocity akc , and a proper characterization of this double dependence, permit the collapse of all the data measured by the array of ultrasonic anemometers. In section 2, we summarize the experimental setup and describe the environmental conditions. In section 3, we present the measurements of the wave-induced velocities and their dependence on the spectral wave age $c(\omega)/U(z)$ and the nondimensional height kz , and we introduce a new parameterization for this dependence. Finally, in section 4, we review and discuss our results.

2. The experiment

a. Experimental setup

The measurements described here were collected from the Floating Instrument Platform (R/P *FLIP*)

moored approximately at the center of the triangle formed by the islands of San Nicholas, Santa Catalina, and San Clemente off the coast of Southern California ($33^{\circ}13.202'N$, $118^{\circ}58.767'W$), in water 1160 m deep from 7 to 22 November 2013, during the ONR Southern California 2013 (SoCal2013) experiment. A telescopic mast was deployed at the end of the port board boom approximately 18 m from the 9-m-diameter hull of R/P *FLIP* (Figs. 1 and 2). The telescopic mast consists of four sections that slide into each other. Each section is approximately 3 m long. While the top section (section 4 in Fig. 2) was tightly coupled to the boom, the extension of each section underneath the boom (sections 1, 2, and 3, section 1 being the lowest) was adjustable. Each section of the mast was equipped with an ensemble of instruments deployed to measure the properties of the airflow above the ocean. Sections 1, 2, 3, and 4 have a 2-, 3-, 4-, and 5-in. square hollow section, respectively. A set of rigging lines connected sections 1, 2, and 3 to the hull of R/P *FLIP* to constrain the horizontal displacement of the mast.

The top section (section 4) of the mast, lengthened by a 2-m vertical pole (with a 2-in. square cross section), was equipped at its highest point with a 3D sonic anemometer (Campbell CSAT3) and with an open-path infrared hygrometer CO₂ sensor (LICOR 7500). These two instruments were mounted on a horizontal pole (with a 2-in. cross section) perpendicular both to the mast and the boom, 1 m away from the mast. At the intersection between the mast and the horizontal pole were mounted a 6-degrees-of-freedom inertial measurement unit [IMU; MEMSIC Attitude Heading Reference System (AHRS) 400] and a relative humidity–temperature sensor (Campbell HC2S3). All these instruments were located about 3 m above the walkway of the boom. As for section 4, each moving section 1–3 of the mast was equipped, at its base, with a 3D sonic anemometer CSAT3, an IMU, and a humidity–temperature sensor (HC2S3). The main differences between the moving sections and section 4 are that the moving sections are not equipped with a hygrometer CO₂ sensor, the IMU model is different (Xsens MTi 300), and the IMU is mounted directly behind the anemometer. In addition to these instruments, the lowest section of the mast was equipped with a 3D sonic anemometer (Gill R3-50) mounted upside down directly below the lowest point of the mast. Hence, the measuring volumes of the Gill and the lowest CSAT3 were separated by 0.85 m in the vertical direction and 1 m in the horizontal direction. Aside the base of the Gill, a single-point laser altimeter (MDL ILM-500) was mounted to monitor the distance between the bottom of the mast and the sea surface. This laser altimeter was

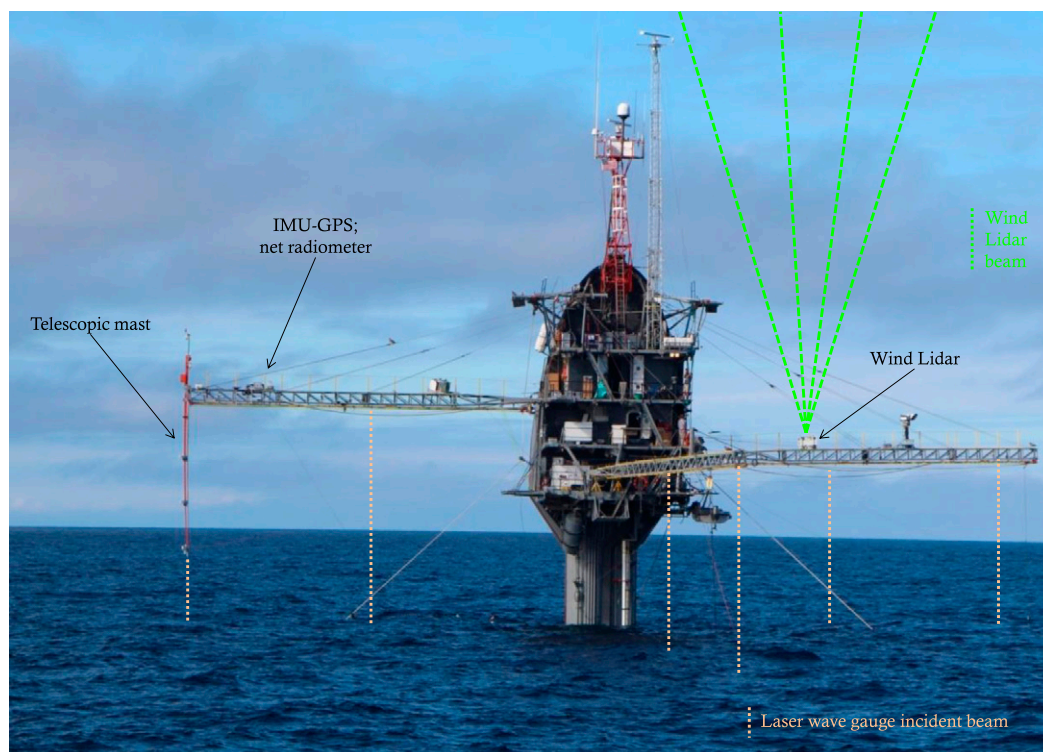


FIG. 1. Experimental setup on R/P *FLIP*. Details of the telescopic mast are presented in Fig. 2. The following instruments were mounted on the booms of the R/P *FLIP*: IMU/GPS (SPAN-CPT, Hemisphere), laser wave gauges (ILM-500), net radiometer (CNR1), and wind lidar (Windcube).

also used as a wave gauge. This setup ensured that all four CSAT3 anemometers were strictly one above the other.

The total extension of the mast was controlled by an electrical winch, while the relative extension of each section was adjusted with a set of rigging lines, manually controlled from the hull of R/P *FLIP*. The extension of the mast was set to bring the lowest instruments as close as possible to the mean sea level (MSL) while preserving the sensors' integrity and distributing the instruments along the vertical axis. Thus, while the highest anemometer remained at 14.8 m (± 0.2 m) above MSL, the lowest anemometer was positioned at an adjustable height, as low as 2.6 m from the MSL (see Fig. 3b).

Reference values of humidity and temperature were provided by Campbell HC2S3 sensors. The hygrometer CO₂ instrument (LICOR 7500), which is also equipped with a pressure sensor, was used to measure the fast fluctuations of the water vapor density and the absolute pressure of the air. Each sonic anemometer measured the three components of the wind.

The temperature–humidity sensors, the hygrometer CO₂ sensor, and the sonic anemometers were sampled at 20 Hz. The laser altimeter is internally sampled at

12 kHz and was averaged down to 100 Hz. The MEMSIC IMU was sampled at 20 Hz, while the Xsens IMUs were sampled at 50 Hz.

In addition to the instruments mounted on the mast, an array of five laser wave gauges (MDL ILM-500, sampled at 100 Hz) located on the starboard, port, and face booms of R/P *FLIP* were deployed to measure the directional spectrum of the sea surface displacement. A Global Navigation Satellite System (GNSS) and Inertial Navigation System (INS; NovAtel SPAN-CPT) was deployed to measure the motion of R/P *FLIP*. This device combines GNSS and INS solutions to deliver position, velocity, and altitude angles with very high accuracy (the accuracy in absolute position is only a few centimeters). The combined solution was sampled at 100 Hz.

A temperature chain (PME T-Chain; 17 thermistors sampled at 0.8 Hz) was deployed from the starboard boom of R/P *FLIP* to monitor the temperature of the first 50 m of the water column. Finally, a wind lidar system (Leosphere Windcube WLS7) was deployed on the starboard boom to measure the vertical profile of the wind every 20 m from 50 up to 400 m above the MSL. The four-beam lidar provided a triangulated measure of the wind components every 4 s.

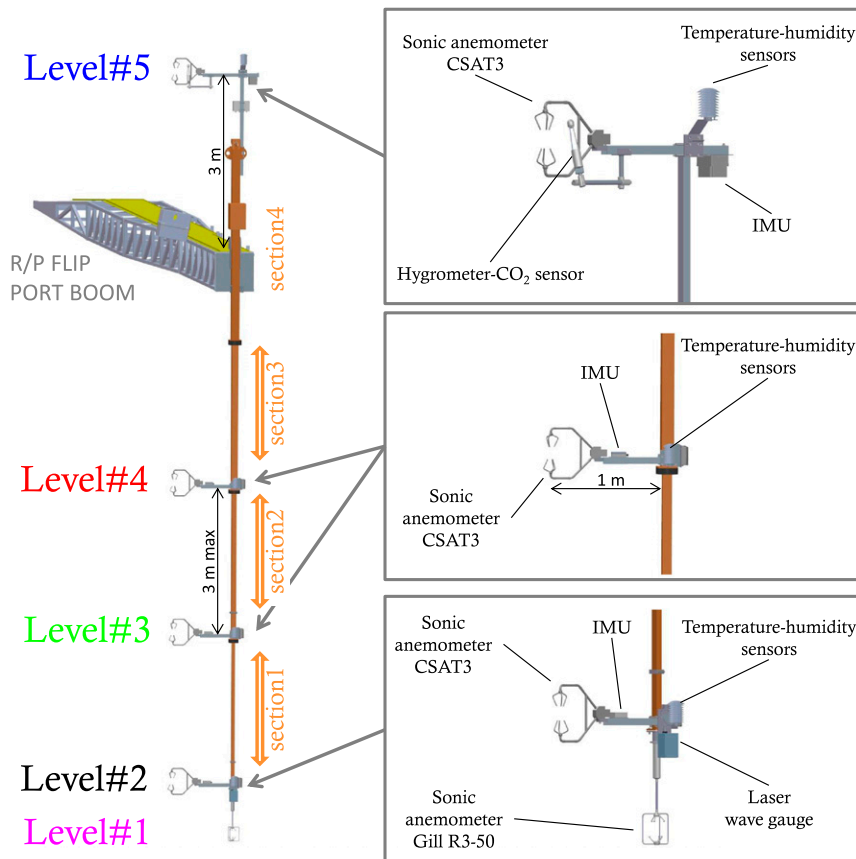


FIG. 2. (left) The telescopic mast with (right) details of the different sections. The following instruments were mounted on the mast: sonic anemometers (CSAT3 and Gill R3-50), temperature–humidity sensors (HC2S3), IMU (AHRS400, MTi300), hygrometer CO₂ sensor (LICOR7500), and laser wave gauges (ILM-500).

b. Data postprocessing and analysis

The sonic velocities and the air–sea interface displacements were corrected to account for the motion of R/P *FLIP*. Those corrections were computed combining solutions from both the IMUs and the SPAN-CPT. The combined solution was used to correct the wind components following Edson et al. (1998). The sea surface elevations measured by the laser wave gauges were corrected for the vertical displacements of the instruments according to the solutions provided by the SPAN-CPT instrument.

After corrections, the wind vector was projected onto a reference frame aligned with the mean direction of the wind using the double-rotation method (Wilczak et al. 2001). This method ensures that the mean vertical velocity is null over 30-min records. Turbulent fluxes of momentum, heat, and water vapor were computed using the covariance method over the same 30-min windows. This time window ensures sufficient statistical reliability in the wind stress and spectral estimates. To avoid the

influence of nonstationary effects on the flux estimates, linear trends in the wind velocity were removed before the computation of the fluctuations. The spectral functions (spectrum, cross-spectrum, phase, and squared coherence) used to derive the products presented below were obtained from fast Fourier transforms (FFTs) using 100-s sliding windows (with a 50-s overlap) over each 30-min record. With signals sampled at 20 Hz, the frequency resolution of the spectral functions is 0.01 Hz. For each anemometer n , the mean wind speed $U_n = U(z_n)$ at the height z_n was computed over the same 30-min record. Using U_n , z_n , the frequency f , and the dispersion relationship for linear gravity waves in deep water, we defined the spectral wave age c/U_n and the normalized (or spectral) height kz_n as follows:

$$\frac{c}{U_n} = \frac{c}{U(z_n)} = \frac{g}{2\pi f U(z_n)}, \quad \text{and} \quad (1)$$

$$kz_n = \frac{4\pi^2 f^2 z_n}{g}. \quad (2)$$

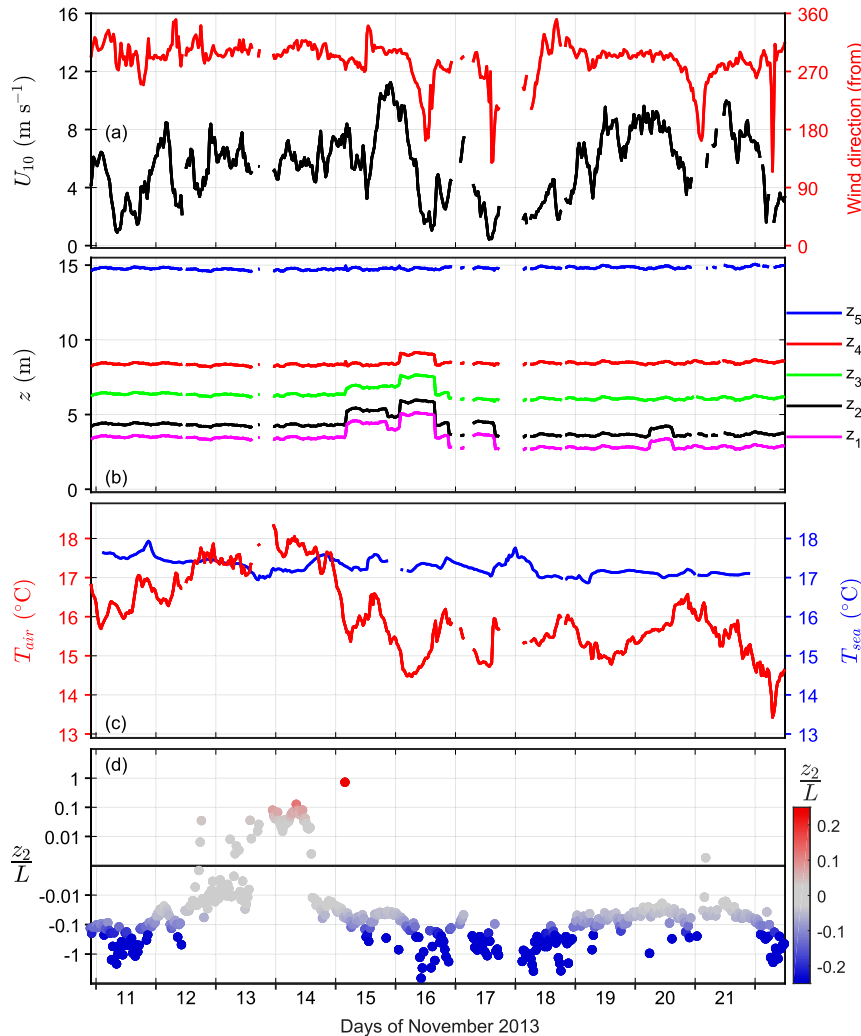


FIG. 3. Environmental conditions of the marine atmospheric boundary layer: (a) U_{10} (black line) and wind direction (from; red line). (b) Heights of the sonic anemometers relative to the mean sea level. (c) Air temperature at $z = z_2$ (red line) and sea temperature at $z \sim -0.5$ m (blue line). (d) Stability parameter z_2/L with L defined in Eq. (4). All the data points are 30-min averages.

Using the same dataset, Grare et al. (2016) showed wind speed discrepancies between measurements from the CSAT3 and the Gill R3-50. They found that differences in the mean wind speed could reach up to 4%, a few degrees in the mean wind direction, up to 5% for the standard deviation of the vertical wind component w' , and up to 20% for the friction velocity. These differences were mainly correlated to the azimuthal angle of the wind relative to the instruments. A portion of these differences were attributed to the transducer's shadowing attenuation occurring on the CSAT3. After correction for this effect, the differences were reduced but the dependence on azimuthal angle of the wind remained. Based on the results from

Grare et al. (2016), we expect to observe discrepancies between the CSAT3 and the Gill R3-50 measurements of the amplitude of the wave-induced velocities to be less than 5%; such discrepancies remained within the scatter of the data, and we believe that they do not alter the conclusions of this manuscript. However, since the discrepancies for the friction velocity could reach up to 20%, discrepancies for the wave-induced momentum flux could be more than 40%. Therefore, analysis and results of the wave-induced momentum flux are not presented in this manuscript. Data from the CSAT3s presented here were corrected for the transducer's shadowing attenuation using the method described in the appendix of Grare et al. (2016).

Finally, 30-min records when the sonic anemometers were located in the wake of the hull of R/P *FLIP* or in the wake of the mast were discarded from the analysis. The wake from the hull of R/P *FLIP* was assumed to be contained within a $\pm 45^\circ$ segment about the port boom. Similarly, the wake from the mast was assumed to be contained within a $\pm 45^\circ$ segment about the direction the CSAT3s were pointing to.

To further analyze the data, the wave-induced velocities were computed. Following [Hussain and Reynolds \(1970\)](#), under the influence of surface waves, we can decompose the fluctuating components of the wind $u_i(t)$ as follows:

$$u_i(t) = \bar{u}_i + \tilde{u}_i(t) + u'_i(t), \quad i = 1, 2, 3, \quad (3)$$

where \bar{u}_i is the mean value, \tilde{u}_i is the wave-induced component, and u'_i is the turbulent component. In the reference frame aligned with the mean direction of the wind, $u_1 = u$ is the streamwise component, $u_2 = v$ is the cross-wind component, and $u_3 = w$ is the vertical component. To extract the wave-induced components, we used the technique developed by [Veron et al. \(2008, 2009\)](#), which uses the cross-spectral functions between the wind components and the vertical displacement of the sea surface. See also [Wu et al. \(2018\)](#).

c. Environmental conditions

[Figure 3](#) shows the variation of statistical parameters of the marine atmospheric boundary layer (MABL) during the SoCal2013 experiment. The horizontal axis represents the date in days from 11 to 21 November 2013 using the coordinated universal time (UTC). Data points are 30-min averages. The data presented herein after do not include measurements performed prior to 11 November 2013 because all the instruments described in the previous section were not fully operational until then. [Figure 3a](#) shows the mean wind speed at 10 m U_{10} and the direction of the wind ϕ . The wind speed U_{10} was calculated by linear interpolation of the wind speed measured by the two anemometers located directly below and above 10 m, that is, using sonic anemometers at level 4 and level 5. The wind direction ϕ was the average of the wind direction measured by all five anemometers. The difference in wind direction between anemometers was less than $\pm 3^\circ$. The wind speed varied from 0 to 11 m s^{-1} , mostly coming from the west–northwest.

[Figure 3b](#) shows the heights of the sonic anemometers during the course of the experiment. These heights are relative to the MSL. The mast was retracted when the waves could potentially hit and damage the lowest anemometer (e.g., on 15 and 16 November 2013).

[Figure 3c](#) shows the variations of the air and the sea temperatures. The air temperature was measured at

$z = z_2$ (see [Fig. 3b](#)) and the sea temperature at $z \sim -0.5 \text{ m}$. Except on 13 and 14 November 2013, the sea was warmer than the air, which is favorable for unstable conditions. [Figure 3d](#) shows the variations of the stability parameter z_2/L , where L is the Monin–Obukhov length ([Monin and Obukhov 1954](#)) measured at the height z_2 by the anemometer collocated to the lowest humidity–temperature sensor. The L is defined as follows:

$$L = -\frac{u_{*2}^3 \overline{\theta'_{v2}}}{\kappa g w_{v2}' \theta'_{v2}}, \quad (4)$$

where all variables are measured at the same height z_2 . The θ_{v2} is the virtual temperature, u_{*2} the friction velocity, g is the gravity, and the overbar represents an average with respect to time. [Figure 3d](#) confirms that the conditions were unstable for most of the experiment.

[Figure 4](#) presents the time variations of the mean wind speed profiles measured both by the array of sonic anemometers and the wind lidar. The color plot in [Fig. 4a](#) represents the variations of the mean wind speed $U(t, z)$ as a function of both the time and the altitude. Data from the array of sonic anemometers correspond to the lower half of the color plot in the range $2.5 < z < 15 \text{ m}$, while data from the lidar correspond to the upper half of the color plot ($60 < z < 500 \text{ m}$). In [Fig. 4b](#), vertical profiles of the normalized mean wind speed $U_s(t, z)$ are plotted every 8 h with

$$U_s(t, z) = \frac{U(t, z) - U_{\min}(t)}{U_{\max}(t) - U_{\min}(t)}, \quad (5)$$

where $U_{\min}(t)$ and $U_{\max}(t)$ are the local minimum and maximum values, respectively, of $U(t, z)$ at a given time t ; that is, $0 < U_s(t, z) < 1$. This figure shows the variability of the mean wind speed in both time and height. It also highlights the extent of the surface layer that contains enough scatterers to return laser pulses from the lidar. In the first days of the experiment, lidar measurements were only available in the first two hundred meters above the MSL, while a few hours before the windiest event, which occurred on 15–16 November 2013, there is a thickening of this layer that extended up to 500 m some time after the wind event passed by our location. [Figure 4b](#) shows the variability of the vertical profiles during the course of the experiment. It also shows that many profiles display a concave or convex curve, meaning that these profiles deviate from the straight line of the logarithmic boundary layer. This highlights the limits of the logarithmic shape assumption and how statistical values based on best-fit log profiles (such as friction velocity, roughness length, and wind

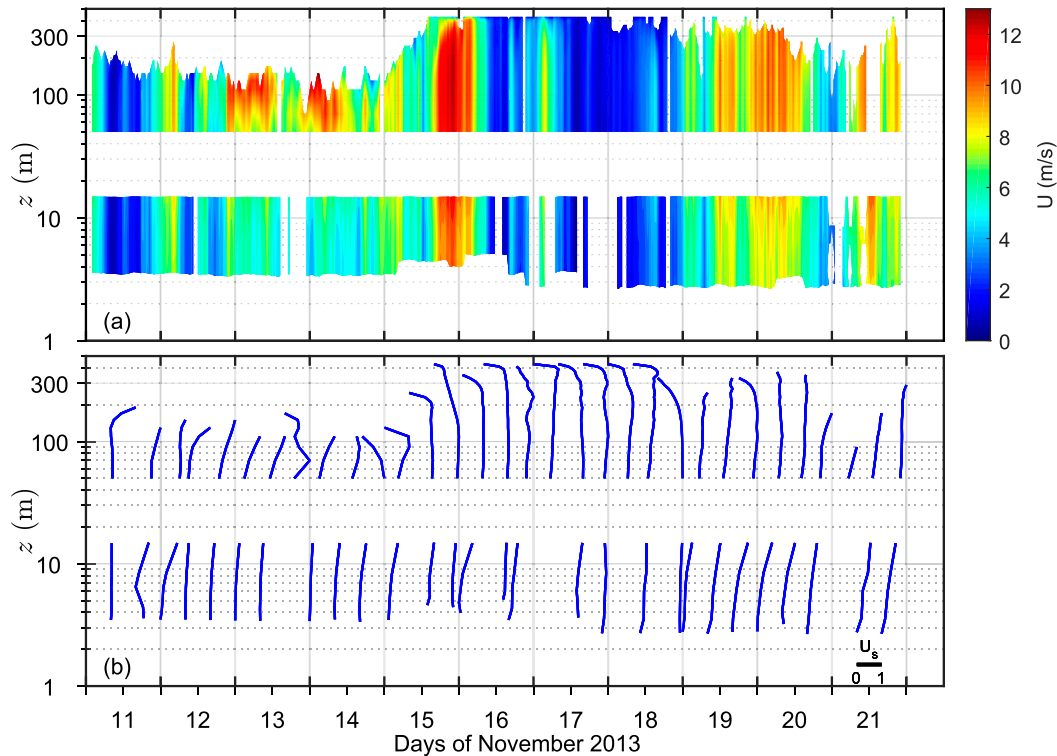


FIG. 4. (a) Mean wind speed as a function of time and height measured by both the sonic anemometers on the telescopic mast ($2.5 < z < 15$ m) and the lidar ($60 < z < 500$ m). (b) Vertical profiles of the normalized mean wind speed $U_s(z)$ plotted every 8 h with $U_s(t, z) = [U(t, z) - U_{\min}(t)]/[U_{\max}(t) - U_{\min}(t)]$, where $U_{\min}(t)$ and $U_{\max}(t)$ are the minimum and maximum values, respectively, of the vertical profile of the mean wind speed $U(t, z)$; that is, $0 \leq U_s(t, z) \leq 1$. The extent of the range $[0, 1]$ is reported in the bottom right corner of the panel. For both panels, data are 30-min averages.

speed at 10 m) can be sensitive to the height of the measurement.

For each 30-min record, the omnidirectional frequency spectrum $S_{\eta\eta}(f)$ and the directional frequency spectrum $S(f, \theta)$ of the surface elevation were computed. An example of these wave spectra (at 0230 UTC 11 November 2013) is reported in Fig. 5. The omnidirectional spectrum was computed for each individual single-point wave gauge (red curve in Fig. 5a), while the directional spectrum was computed from the array of wave gauges using the WAFO MATLAB library (WAFO Group 2000) for frequencies in the range 0.03–0.4 Hz. The omnidirectional spectrum can also be computed from the azimuthal integration of the directional spectrum $S_{\eta\eta} = \int S(f, \theta) d\theta$ (black curve in Fig. 5a).

For the directional spectrum (Figs. 5b,c), the frequency scale corresponds to concentric circles that are logarithmically spaced, and the azimuthal direction corresponds to the direction of propagation of the waves. The colored contours delimit the different partitions of the wave field. This example emphasizes the utility of the directional spectrum, as in the omnidirectional spectrum only three peaks are distinguishable, while four wave partitions are

clearly visible in the directional spectrum. The partitioning of the wave field was performed running a script based on the methods described in Hanson and Phillips (2001) and Portilla et al. (2009). As suggested in Portilla et al. (2009), we applied to the directional spectra a 2D noise-removal filter before partitioning the spectrum using a “watershed” algorithm.¹ In Fig. 5b, the raw directional spectrum is plotted while its filtered form is plotted in Fig. 5c.

The example presented is characteristic of the conditions encountered during the experiment. The wave field was formed by the superposition of four main components:

- Wind waves (delimited by the orange contour) directly associated with local winds, with frequencies generally higher than 0.1 Hz.

¹ The “watershed” algorithm, which treats each directional spectrum like a topographic map, with the power spectral density of each point representing its height, finds the lines that run along the tops of ridges and separates adjacent drainage basins that correspond to adjacent partitions of the wave field.

- Local north–northwest swell (delimited by the green contour), residual of wind waves generated upwind of our location [say, $O(100)$ km], which propagated to our position after the wind died. These waves were passing by for short periods of time (less than 2 days) with frequencies ranging between 0.08 and 0.15 Hz.
- Old (remote) north–northwest swell (delimited by the black contour) generated by storms in the North Pacific Ocean, passing by our location for up to four days, with the longest waves (down to ~ 0.06 Hz) arriving before the shorter ones (up to ~ 0.1 Hz).
- Swell from the Southern Hemisphere (delimited by the purple contour) generated by remote storms in the Southern Hemisphere, with frequencies in the range of 0.07–0.1 Hz.

For each 30-min record and for each wave component defined by an ensemble of pairs (f, θ) bounded by the contour \mathcal{A} , we computed the following:

- The mean frequency²

$$\bar{f} = \frac{\iint_{\mathcal{A}} f S(f, \theta) df d\theta}{\iint_{\mathcal{A}} S(f, \theta) df d\theta} \quad (6)$$

- The mean direction

$$\bar{\theta} = \tan^{-1} \left(\frac{\iint_{\mathcal{A}} S(f, \theta) \sin \theta df d\theta}{\iint_{\mathcal{A}} S(f, \theta) \cos \theta df d\theta} \right) \quad (7)$$

- The mean energy

$$\Delta E = \rho_w g \iint_{\mathcal{A}} S(f, \theta) df d\theta \quad (8)$$

Each pair $(\bar{f}, \bar{\theta})$ is reported in Figs. 5b and 5c as a solid colored point.

Figure 6a shows the omnidirectional spectrogram of the surface displacement. The $S_{\eta\eta}(f)$ is computed from the directional spectrum, and the color scale is logarithmic. The plot shows that throughout the duration of the experiment, different wind-wave events occurred, and swell was always a significant component of the wave field.

Figure 6b shows the significant wave height H_s and the mean wave age C_p/U_{10} , where C_p is the phase speed at the peak of the wave elevation spectrum. The significant

wave height was computed from the directional spectrum as follows:

$$H_s = 4 \sqrt{\iint S(f, \theta) df d\theta} = 4 \sqrt{\int S_{\eta\eta}(f) df}. \quad (9)$$

The significant wave height remained small, less than about 1.5 m, for most of the experiment except on 15 November 2013 and the beginning of 16 November 2013, when it reached 2.5 m, corresponding to a high-wind event. Hence, the wave age C_p/U_{10} was large (greater than 2) for most of the experiment.

The mean frequency \bar{f} and direction $\bar{\theta}$ of each partition of the wave field are reported in Fig. 6c. The relative mean energy of each partition $\Delta E/E$ is shown in Fig. 6d, where $E = \rho_w g \iint S(f, \theta) df d\theta$ is the total wave energy per unit surface area, integrated over all frequencies and directions.

These two bottom panels show that the wave field was quite complex during this experiment, with a superposition of local wind waves, young and old swells from the north–northwest, and long swell from the south where the relative energy contribution of each wave component varies strongly over time.

The plots presented in Figs. 3 and 6 show dropouts in the data (e.g., on 17 November 2013). These dropouts either were the result of the loss of GPS signal from the SPAN-CPT inertial unit because of temporary technical issues or were the result of periods of low wind speeds when the laser wave gauges had low returns from the glassy sea surface. Cases with a percentage of returns less than 12.5% were excluded from our analysis. This 12.5% threshold was selected because we found that below this threshold the temporal and spatial distributions of the returns were too scattered to properly reconstruct the wave profile.

3. Wave-induced fluctuations of the wind

a. Coherence and phase

Figures 7 and 8 show 11 days of the squared coherence and phase shift between the waves and the wind measured by each anemometer. The left panels show the coupling with the horizontal fluctuations u_n , while the right panels show the coupling with the vertical fluctuations w_n . For the horizontal velocity (and similarly for the vertical velocity), the squared coherence $\gamma_{\eta u}^2$ is the magnitude of the squared cross-spectral density $C_{\eta u}$ normalized by the product of the wave spectrum $S_{\eta\eta}$ and the velocity spectrum S_{uu} . The phase shift $\Phi_{\eta u}$ is the argument of $C_{\eta u}$. The top panels refer to the highest anemometer while the bottom panels refer to the lowest one. The right vertical axis is the frequency, and the left vertical axis is the phase speed of the waves $c = g/(2\pi f)$.

²Note that the definition is different from the one used in Hanson and Phillips (2001).

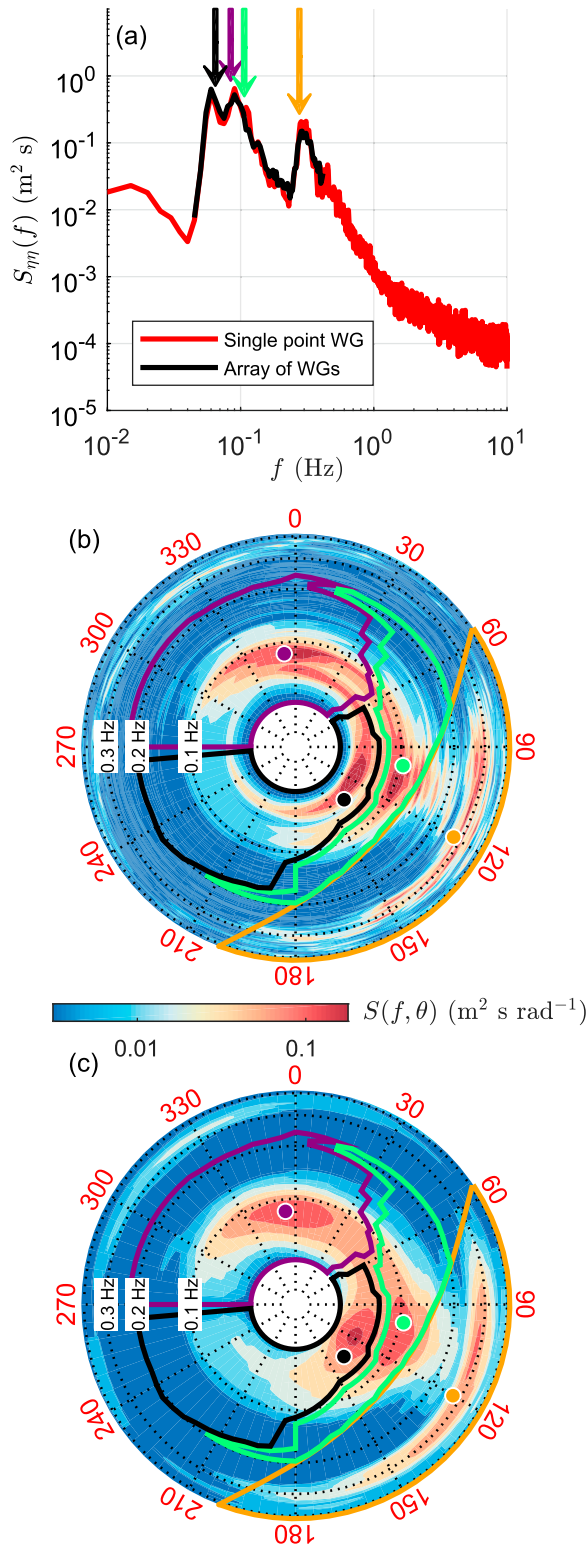


FIG. 5. Example of the omnidirectional and directional spectra of the wave field from 30-min records starting at 0230 UTC 11 Nov 2013. (a) Omnidirectional spectra from measurements of the laser wave gauge located at the bottom of the telescopic mast (red) and

For each panel, the black line represents the mean wind speed at the height of the corresponding anemometer $U_n = U(z_n)$. The black line also corresponds to the speed of the waves, which have the corresponding anemometer located at their critical height. The critical height was introduced by Miles (1957) in his quasi-laminar inviscid model built on the concept of resonant interaction between wind and waves. In this model, the equations of motion governing a small perturbation (assumed to be linearly correlated to the surface waves) of a two-dimensional shear flow $U(z)$ in an inviscid and incompressible fluid leads to the inviscid form of the Orr–Sommerfeld equation. This equation has a singularity where the wind speed $U(z_c)$ equals the phase speed c of the waves, that is, at the height z_c of the critical layer, which implies that the rate at which energy and momentum are transferred to a wave of speed c depends on quantities at the critical height z_c (see also Lighthill 1962; Hristov et al. 2003; Young and Wolfe 2014). Wave-coherent fluctuations at phase speeds greater than the wind speed (i.e., above the black line in Fig. 7) were measured below the critical layer associated with those waves. The color scale for the squared coherence is logarithmic. For all the anemometers, the squared coherence between the waves and the vertical velocity is greater than the squared coherence between the waves and the horizontal velocity. This observation is consistent with Grare et al. (2013a). We observe a glimpse of the vertical decay of the wave-induced fluctuations as, for both horizontal and vertical fluctuations, the squared coherence is larger closer to the surface. This is particularly true at frequencies associated with wind waves since for the lowest anemometers, we observe patches of high coherence in the proximity of the black line (i.e., at frequencies where the phase speed was close to the wind speed), while the squared coherence remained low at these frequencies at higher elevations. For the top anemometer, high levels of squared coherence (say greater than 0.2) are only observed at frequencies smaller than about 0.2 Hz, while for the lowest anemometer, high coherence is observed at higher

←

by the azimuthal integration of the directional spectrum (black). (b) Directional spectrum from the array of laser wave gauges. (c) Smoothed directional spectrum used to partition the wave field. For the directional spectra, the direction refers to the direction the waves move to and the frequencies correspond to concentric circles logarithmically spaced. The colored boundaries delimit the main partitions of the wave field: southern swell (purple), northern swell (black), local swell (green), and wind waves (orange). The solid colored dots correspond to the mean frequency and direction of each partition.

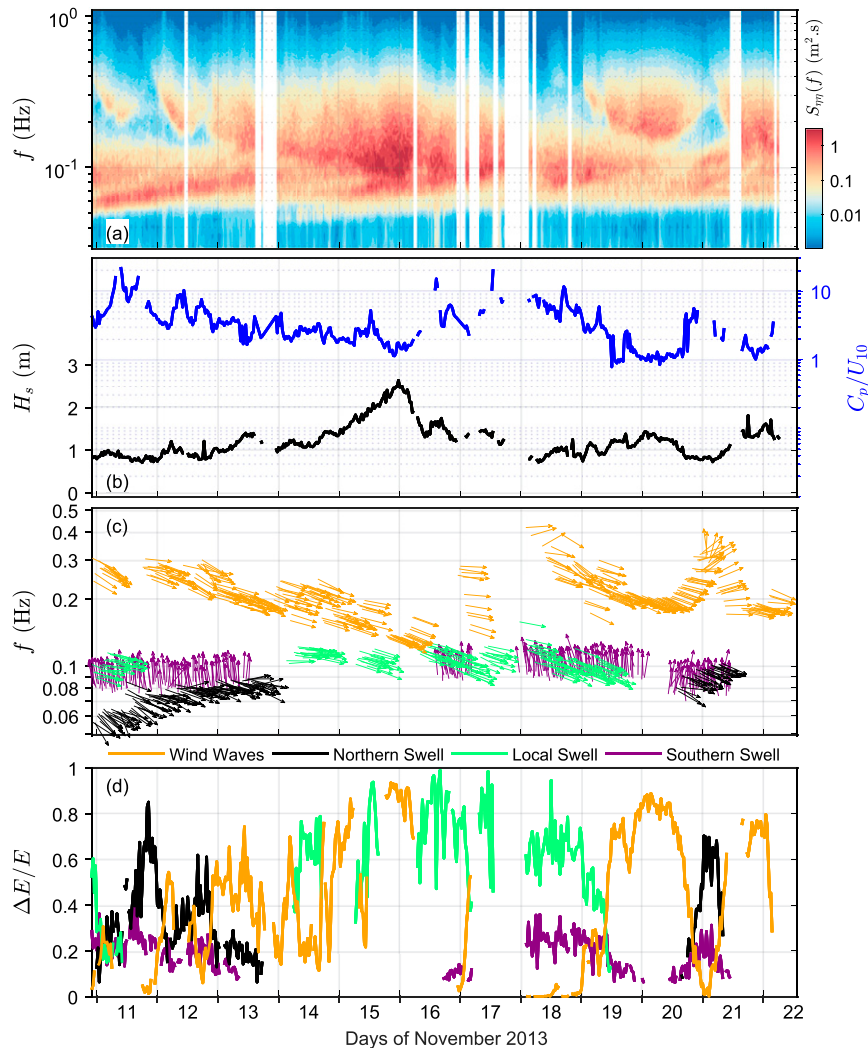


FIG. 6. Characteristics of the wave field during the experiment. (a) Spectrogram of the surface displacement. (b) Significant wave height H_s (black line) and wave age C_p/U_{10} (blue line). (c) Frequencies and directions of the main partitions of the wave field: wind waves (orange arrows), northern swell (black arrows), local swell (green arrows), and southern swell (purple arrows). (d) Relative energy $\Delta E/E$ of the main partitions of the wave field. See Eq. (8) for the definition of ΔE . Colors are as in (c).

frequencies (up to 0.5 Hz) and also when c is close to $U(z)$. Fluctuations associated with both the swell and the wind waves are present in the data. This is most clearly illustrated in Figs. 7e and 7j on 11 November and between 20 and 21 November by the presence of distinctive patches of high coherence. Figure 7 also shows that most of the wave-induced fluctuations measured in this experiment were found below the critical layers as the squared coherence remains small below the black lines (i.e., above the critical layer).

Figure 8 shows that the phase between the waves and the wind is relatively constant below the critical layers, the horizontal component being out of phase (about 180°) with

the waves while the vertical component is in quadrature (about 90°). For most of the data, the phase above the critical layers is very noisy and appears random. This is a direct effect of the low level of coherence square γ^2 observed in Fig. 7 above the critical layers where γ^2 is generally smaller than 0.05. Indeed, the normalized random error of the estimates of the phase $\varepsilon(\hat{\Phi})$ depends directly on the level of coherence square (Bendat and Piersol 2010); for example, for 100-s FFT windows along the 30-min record, $\varepsilon(\hat{\Phi}) \sim 42^\circ$ when $\gamma^2 = 0.05$. Close to the surface, the lowest anemometers measured signals with a level of coherence high enough to observe the sharp change of the phase across the critical layers, especially for

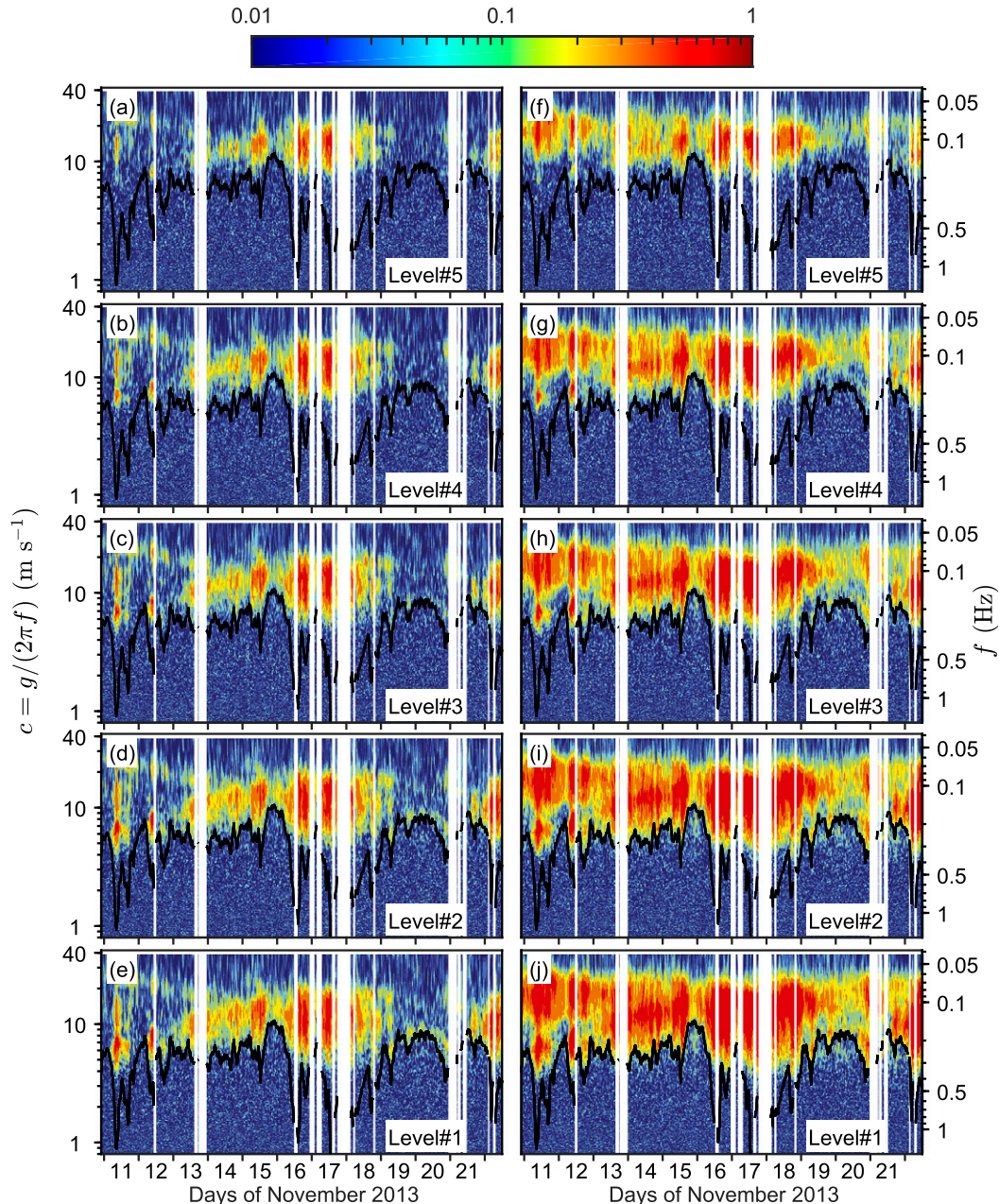


FIG. 7. The squared coherences $\gamma_{\eta u_n}^2$ and $\gamma_{\eta w_n}^2$ between the surface displacement η and the wind components u_n and w_n . (a)–(e) Horizontal velocity. (f)–(j) Vertical velocity. (from bottom to top) Velocities measured by anemometers 1 to 5. The right y axis is the frequency, and the left y axis is the linear phase speed of the waves. The black line is the 30-min mean wind speed $U(z_n)$ at the height of each anemometer. It is also the phase speed of the waves for which the anemometer is at their critical height.

the vertical component, which shifts from $+90^\circ$ to -45° (purple patches on 15–16 November and 19–20 November below the black curve). This is in accordance with the critical layer theory (Miles 1957) and with the measurements from Hristov et al. (2003) and Grare et al. (2013a). Away from the surface, the coherence above the critical layers is too weak to accurately calculate the phase

between the wind modulations and the waves. Therefore, the sharp change of phase across the critical layers cannot be observed with the highest anemometers.

b. Selection of the wave-coherent fluctuations

To study the variation of the wave-induced velocities with wind forcing and height, we have selected fluctuations

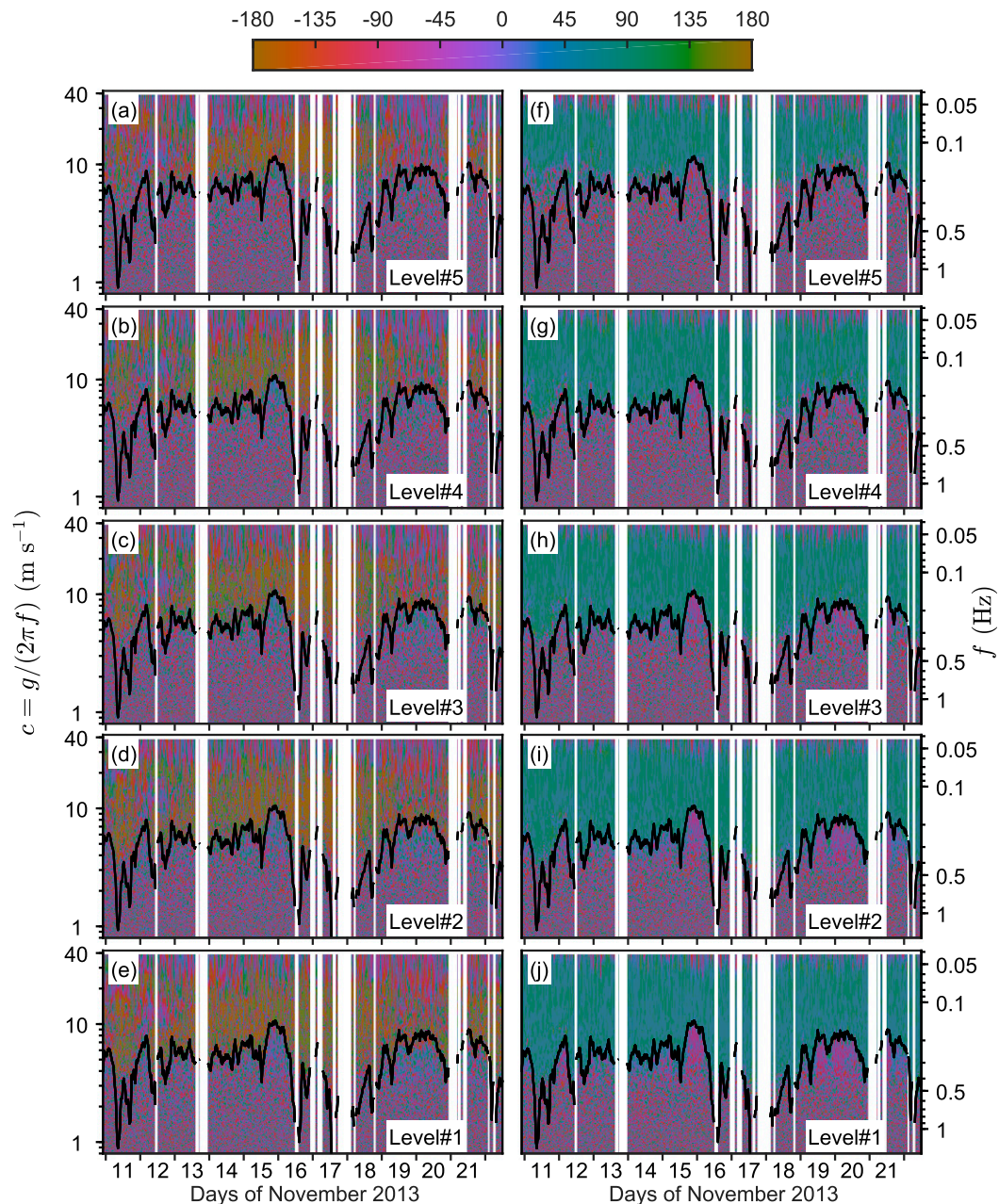


FIG. 8. The phase shift $\Phi_{\eta u_n}$ and $\Phi_{\eta w_n}$ between the surface displacement η and the wind components u_n and w_n . The order of the panels, the axes, and the black lines are as in Fig. 7. The phase is relatively constant below the critical layers (above the black lines), the horizontal component being out of phase (about 180°) with the waves while the vertical component is in quadrature (about 90°). Close to the surface, the lowest anemometers are able to measure coherent signals across the critical layers where a sharp change of the phase is observed, especially for the vertical component which shifts from $+90^\circ$ to -45° .

of the wind coherent with the waves as done in Hare et al. (1997) and Grare et al. (2013a), that is, according to the level of squared coherence between the surface elevation and the velocities. To minimize the effect of spurious noise and to ensure reliable wave-induced signals, only the frequencies for which the squared coherence $\gamma_{\eta u_i}^2$ was above a

conservative threshold of 0.2 were included in the final dataset. The value of this threshold is set arbitrarily in order to gather the maximum number of data points available for the analysis while limiting the scatter in the data [this threshold was set to 0.1 in Hare et al. (1997) and Grare et al. (2013a)]. The value of 0.2 provides a good

compromise for the current dataset. We have also restricted the selection to frequencies in the range 0.06–0.5 Hz to ensure rejecting wind fluctuations correlated with the heave and the tilt motions of *FLIP* (around 0.04 and 0.02 Hz, respectively; see [Smith and Rieder 1997](#)), which do not correspond to the physical coupling between the airflow and the wavy surface.

c. Double dependence and parameterization

[Hare et al. \(1997\)](#) examined the structure of the atmospheric wave-induced variables as a function of the wind forcing u_*/c (or the wave age c/u_*) and the normalized height kz . They formed their approach guided by the expression of the wave growth parameter β forced by wind through the form drag only:

$$\beta = \frac{\dot{E}}{E} = \frac{\tau_w c}{\frac{1}{2} \rho_w g S_{\eta\eta}}, \quad (10)$$

where E is the wave energy per unit surface area, the overdot is time derivative, and the form drag τ_w is equal to the correlation between the wave-induced pressure perturbation at the surface and the slope of the waves. Using results from [Plant \(1982\)](#), [Al-Zanaidi and Hui \(1984\)](#), and [Jacobs \(1987\)](#), they assumed that the single most important parameter to describe wind-wave interaction is the dimensionless forcing u_*/c . They justified the vertical dependence of the pressure and velocity fields on the normalized height kz from the results of [Snyder et al. \(1981\)](#) and [Jacobs \(1987\)](#), who showed that the wave-induced pressure–slope correlation has an exponential decay $\exp(-\alpha kz)$ with α close to 1. Assuming that the wave-induced motions are linearly related to the surface displacements $\eta(x, t)$, the amplitude of these motions are proportional to the magnitude of the wave displacement described by the omnidirectional wave spectrum $S_{\eta\eta}$. Using the wavelength λ and the phase speed c of the waves as the typical length and velocity scales, they ended up with the following relationship between the nondimensionalized wave-induced velocities and some function $N_{\eta u_i}$, which depends on both the wind forcing u_*/c and the dimensionless height kz :

$$N_{\eta u_i} \left(\frac{u_*}{c}, kz \right) = \frac{C_{\eta u_i} \lambda}{S_{\eta\eta} c}, \quad (11)$$

where $C_{\eta u_i}$ is the complex cross spectrum between the vertical surface displacement and the wind component u_i , $u_1 = u$ is the streamwise component, $u_2 = v$ is the crosswise component, and $u_3 = w$ is the vertical

component. Building from the results of [Hristov et al. \(2003\)](#) and [Grare et al. \(2013a\)](#), who have highlighted the strong influence of the critical layer on both the amplitude and the phase of the wave-induced velocity fields, here we support the hypothesis that the local wave age $c/U(z)$ should be used in lieu of the wind forcing u_*/c to better characterize the effect of the critical layer. Furthermore, in order to satisfy the kinematic conditions at the air–sea interface, the wave-induced components of the airflow should match, at the surface, the orbital velocity of waves of amplitude $O(akc)$ at leading order. Therefore, wave-induced velocities can be directly nondimensionalized by the orbital velocity akc . Using this new scaling, and focusing on the amplitude of the wave-induced velocities, we obtain a new relationship where the dimensionless wave-induced velocity depends only on the local wave age $c/U(z)$ and the dimensionless height kz :

$$N_{\eta u_i}^* \left[\frac{c}{U(z)}, kz \right] = \frac{|\tilde{u}_i|}{akc} = \frac{\sqrt{S_{\tilde{u}_i \tilde{u}_i}}}{\sqrt{S_{\eta\eta}} kc} = \frac{|C_{\eta u_i}|}{S_{\eta\eta} kc}. \quad (12)$$

As the wave field was complex in our experiment with waves propagating in different directions, each wave component is likely to generate its own wave-induced field of velocity in its direction of propagation. To account for the three-dimensional properties of the wave-induced airflow, we regrouped the streamwise \tilde{u}_1 and crosswise \tilde{u}_2 wave-induced velocity components by computing the amplitude of the horizontal wave-induced velocity $|\tilde{u}_h| = \sqrt{|\tilde{u}|^2 + |\tilde{v}|^2} = \sqrt{|\tilde{u}_1|^2 + |\tilde{u}_2|^2}$. Thenceforth, u_i refers either to the horizontal or the vertical velocity (u_h or w , respectively).

[Figure 9](#) shows the variations of the amplitude of the dimensionless wave-induced horizontal ($|\tilde{u}_h|$ in the left panels) and vertical ($|\tilde{w}|$ in the right panels) velocities as a function of the dimensionless height kz_n for each measurement level. The amplitude of the dimensionless wave-induced velocities $|\tilde{u}_i/akc|$ were estimated from the norm of the spectral transfer function $|T_{\eta u_i}(c)|$ between wind and waves normalized by the angular frequency $\omega(c) = kc$:

$$\frac{|\tilde{u}_i|}{akc}(c) = \frac{|\tilde{u}_i(c)|}{a(c)\omega(c)} = \frac{|S_{\tilde{u}_i}(c)|}{\omega(c)S_{\eta\eta}(c)} = \frac{|T_{\eta u_i}(c)|}{\omega(c)}. \quad (13)$$

Data from the five sonic anemometers are reported from top to bottom, with [Figs. 9a and 9b](#) representing the highest anemometers (level 5) and [Figs. 9i and 9j](#) representing the lowest anemometer (level 1). Data points

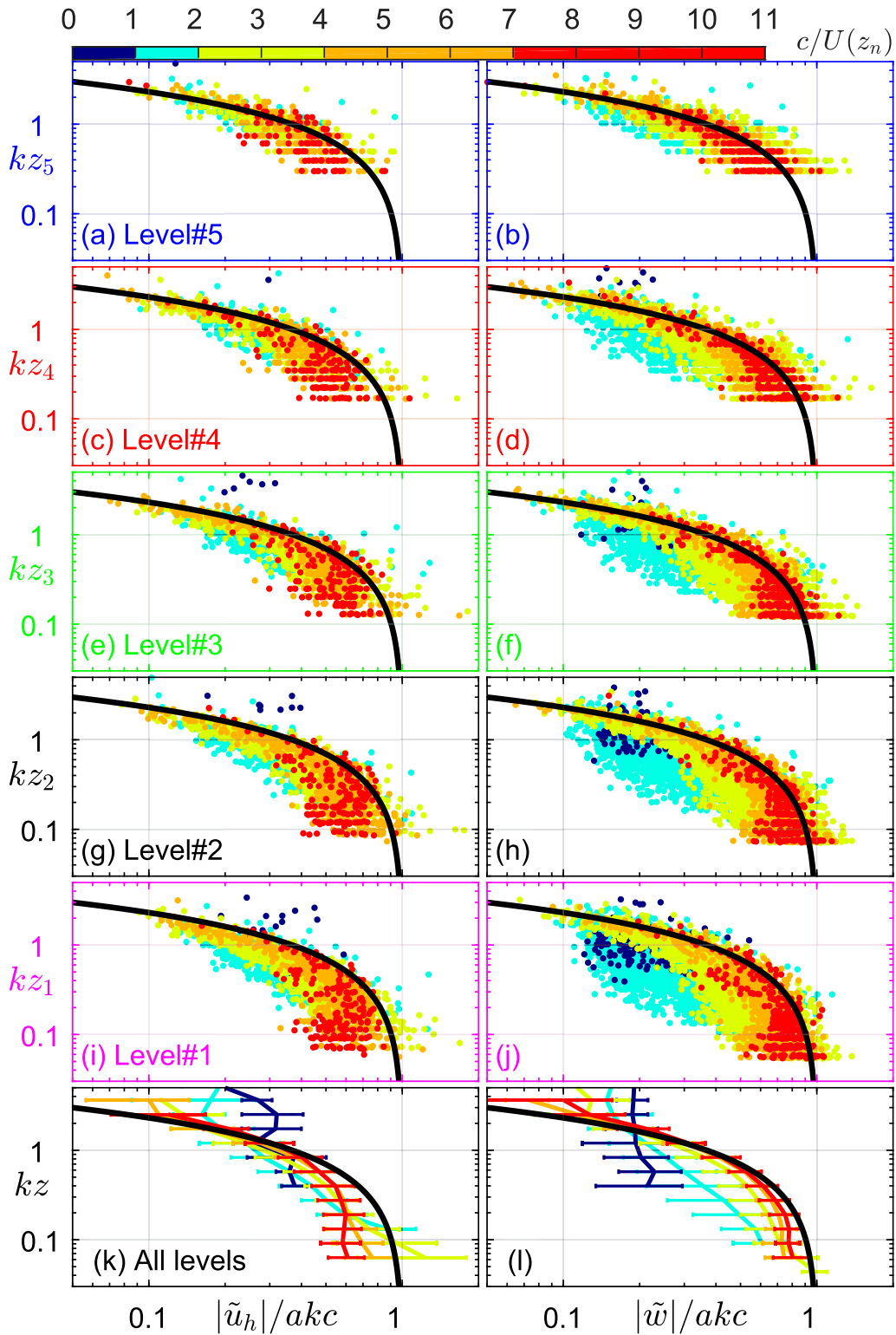


FIG. 9. (a)–(j) The amplitude of the dimensionless wave-induced velocities (left) $|\tilde{u}_h(z_n)|/akc$ and (right) $|\tilde{w}(z_n)|/akc$ as a function of the normalized height kz for each level. Data are colored depending on spectral wave age ranges $c/U(z)$. (k), (l) Averaged profiles from data from all levels, bin-averaged by spectral wave age with the standard deviation within each bin drawn with the horizontal error bars. In each panel, the solid black line is the exponential function $\exp(-kz)$.

are colored by bins of the spectral wave age $c/U(z_n)$ according to the color bar at the top of the figure. In Figs. 9k and 9l, data from all anemometers have been combined and bin averaged per dimensionless height bins for each wave age bin. The error bars represent the standard deviation of the data within a dimensionless height bin. For each panel, the solid black curve is the exponential function $\exp(-kz)$. For all anemometers, data show that when the wave age becomes large, the vertical profiles of the wave-induced velocity amplitude tend toward the exponential decay $\exp(-kz)$. However, for smaller values of the wave age (less than 2), the scatter of the data is quite large; for example, for the vertical component measured by the lowest anemometer (Fig. 9j), data with a wave age between 1 and 2 (i.e., for data measured close to the critical layers) spread over almost one decade when kz is about 0.5. This highlights the influence of the critical layers on the wave-induced velocities whose amplitude decreases abruptly in the vicinity of the critical layer. Note that for low wind cases the wave-induced fluctuations can contribute to a large fraction of the total fluctuations, up to 90% (not shown here).

The double dependence of the wave-induced velocities on both the wave age and the dimensionless height, is presented in the Fig. 10, where the variations of \tilde{u}_h/akc and \tilde{w}/akc as a function of $c/U(z)$ are plotted in Figs. 10a and 10b, while the variations with kz are reported in Figs. 10c and 10d. In this figure, data have been bin averaged individually for each level, where blue is the highest anemometer, and purple is the lowest anemometer. Hereinafter, bin-averaged data with fewer than 10 data points within the bin are not plotted. Raw data are reported in Fig. S1 in the online supplemental material.

Figures 10a and 10b show that the amplitudes of the wave-induced velocities decrease for wave ages close to 1. Figures 10c and 10d show that wave-induced velocities decay with normalized height kz following an exponential law. We show here that for a given wave age, the amplitude of the wave-induced velocities is inversely proportional to the height above the surface. However, in the bottom panels (especially in Fig. 10d), for a given normalized height kz (e.g., $kz = 0.5$), the amplitude of the wave-induced velocity is smaller when measured at low levels than when measured at higher levels. This trend is due to the fact that for a given $kz = k_n z_n = k_m z_m$, where $z_n > z_m$, the wave age at the lower level is smaller than the one at the higher level; that is $c_n/U(z_n) > c_m/U(z_m)$. Therefore, data from the lower anemometer are more affected by the critical layer than are those at higher levels. As shown in Figs. 10a and 10b, in the proximity of the critical layer,

the amplitude of the wave-induced velocities are reduced especially when $c/U(z) < 2$. This critical layer influence explains why the bin-averaged data shown in Fig. 10d present values that are smaller at lower levels than at higher levels.

To decouple the double dependence on $c/U(z)$ and kz , we propose to parameterize the variations of the wave-induced fluctuations with two independent functions $F_i(c/U)$ and $G_i(kz)$, such that

$$\frac{|\tilde{u}_h|}{akc} \left[\frac{c}{U(z)}, kz \right] = A_u F_u \left[\frac{c}{U(z)} \right] G_u(kz) \quad \text{and} \quad (14)$$

$$\frac{|\tilde{w}|}{akc} \left[\frac{c}{U(z)}, kz \right] = A_w F_w \left[\frac{c}{U(z)} \right] G_w(kz), \quad (15)$$

where A_u and A_w are constants close to 1. As demonstrated in our analysis, we can assume that the vertical decay can be described with an exponential function:

$$G_i(kz) = \exp(-\alpha_i kz), \quad (16)$$

where α_i is a constant close to 1. The subscript i is equal to either u or w depending on whether the parameterization is applied to the horizontal or the vertical wave-induced velocity (\tilde{u}_h or \tilde{w} , respectively). For clarity, the subscript will be omitted hereinafter. To characterize the dependence on wave age, we first assume that the decay in amplitude of the wave-induced fluctuations can be described using the inverse wave age $U(z)/c$:

$$F \left[\frac{c}{U(z)} \right] = \left| 1 - \frac{U(z)}{c} \right|. \quad (17)$$

The use of this function is motivated by Miles's (1957) critical layer theory to describe the forcing of the waves by the wind. In this theory, the wave-induced velocities drop rapidly close to the critical layer, where the mean wind speed equals the phase speed of the waves, that is, where $c/U(z) = 1$. Although there is no exact analytical expression for the wave-induced velocities, Lighthill (1957, 1962), Kudryavtsev et al. (2001), and Kudryavtsev and Makin (2004) have shown that to a first approximation $\tilde{u}_i \approx \theta_0(U - c) \exp(-kz)$, where $\theta_0 = ak$ is the slope of the water surface. The constants A and α are estimated by minimizing a squared-difference cost function, and their values are reported in Table 1. The coefficient of determination r^2 between the data and the different parameterizations is also reported in this table. The best-fit regression produces values of A quite close to unity ($A_u = 0.95$ for the horizontal component and $A_w = 1.07$ for the vertical component) when A is unconstrained; however, the exponential decay

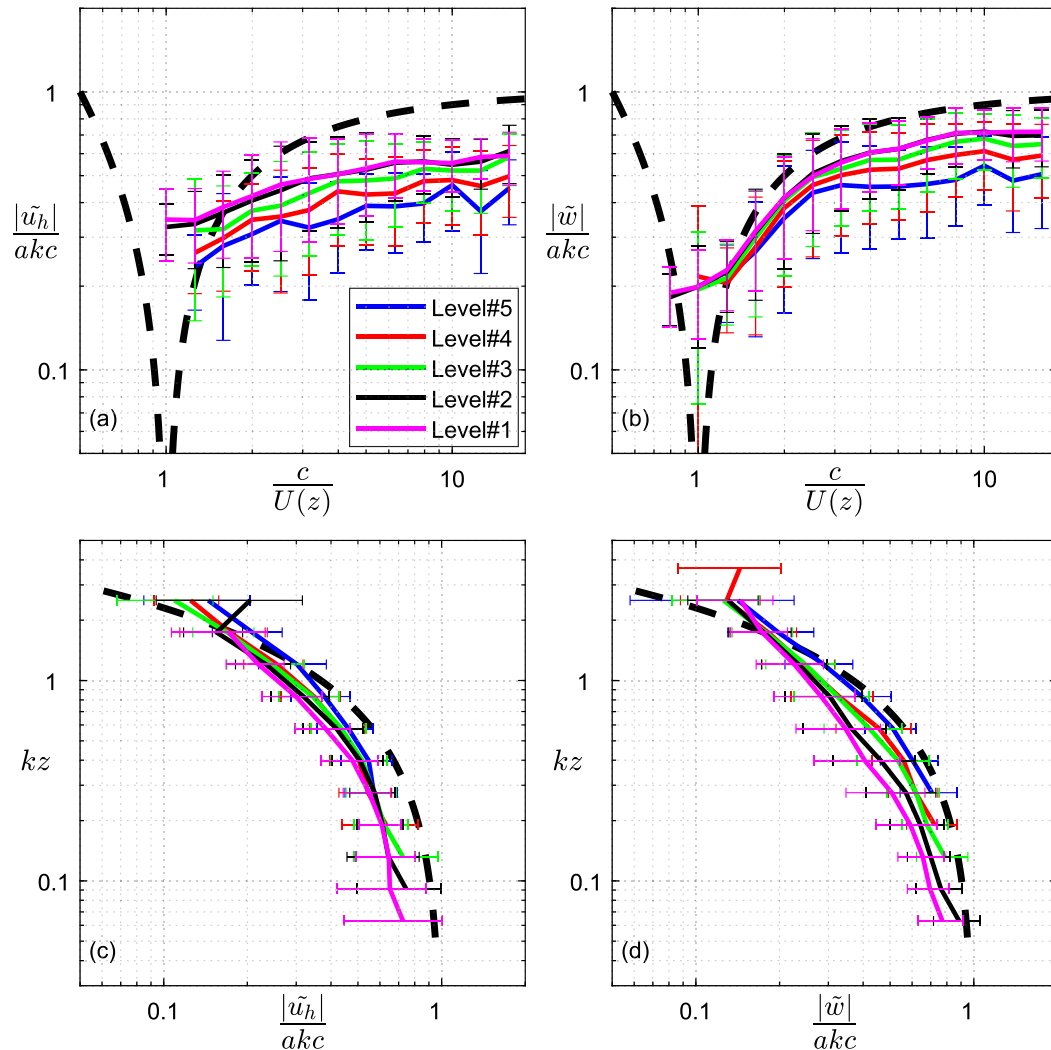


FIG. 10. The bin-averaged amplitude of the (left) horizontal and (right) vertical dimensionless wave-induced velocities, (a),(b) as a function of the spectral wave age $c/U(z)$ and (c),(d) as a function of the normalized height kz , for each level. Error bars correspond to the standard deviation of the data within each bin. The functions $F(c/U) = |1 - U/c|$ in (a) and (b) and $\exp(-kz)$ in (c) and (d) are plotted with dashed black lines.

coefficients α_u and α_w change by about 10%–15% between the case where A is unconstrained and the case where A is set to one.

Figure 11 shows the amplitude of the wave-induced fluctuations scaled by the functions $F[c/U(z)]$ and $G(kz)$ plotted as functions of the wave age and the normalized height in the case where A is set to one. Data are bin averaged for each anemometer subset of records. Raw data are presented in the Fig. S2. In Figs. 11a and 11b, the data have been corrected for their dependence on $G(kz) = \exp(-\alpha_k z)$ with $\alpha_u = 0.77$ for the horizontal wave-induced velocity and $\alpha_w = 0.62$ for the vertical velocity. In these panels the collapse of the data from the five different anemometers is remarkable. Some discrepancies remain as $c/U(z)$ gets close to 1. This is

due to the small number of data points within the bins for this range of c/U ; for example, for level 5 (blue curve) there are only 19 data points within the bin $1 < c/U(z) < 1.5$, leading to a standard deviation (STD) for this bin 40 times greater than the median value of the STD for all bins. Another indicator of the performance of this scaling is the scatter of the data around the bin-averaged curves. Raw data presented in Figs. S1a, S1b, S2a, and S2b show that the scaling to account for the exponential decay with height drastically reduced the spreading of the data. Note that in the top panels, the dashed orange line represents the function $F[c/U(z)] = |1 - U(z)/c|$. The agreement with the data is very good for high $c/U(z)$, where the best-fit curve lies within the error bars of the bin-averaged data. However,

TABLE 1. Best-fit coefficients of proposed wave-induced velocity parameterizations.

| | A_i | α_i | β_i | ζ_i | r_i^2 |
|--|-------|------------|-----------|-----------|---------|
| $\frac{ \tilde{u}_h }{akc} = \left 1 - \frac{U}{c}\right \exp(-\alpha_u kz)$ | | 0.77 | | | 0.38 |
| $\frac{ \tilde{w} }{akc} = \left 1 - \frac{U}{c}\right \exp(-\alpha_w kz)$ | | 0.62 | | | 0.67 |
| $\frac{ \tilde{u}_h }{akc} = A_u \left 1 - \frac{U}{c}\right \exp(-\alpha_u kz)$ | 0.95 | 0.68 | | | 0.38 |
| $\frac{ \tilde{w} }{akc} = A_w \left 1 - \frac{U}{c}\right \exp(-\alpha_w kz)$ | 1.07 | 0.74 | | | 0.68 |
| $\frac{ \tilde{u}_h }{akc} = A_u \left[1 - \beta_u \exp\left(-\zeta_u \left \frac{c}{U} - 1\right \right)\right] \exp(-\alpha_u kz)$ | 0.76 | 0.85 | 0.32 | 0.96 | 0.64 |
| $\frac{ \tilde{w} }{akc} = A_w \left[1 - \beta_w \exp\left(-\zeta_w \left \frac{c}{U} - 1\right \right)\right] \exp(-\alpha_w kz)$ | 0.85 | 0.83 | 0.66 | 1.00 | 0.76 |
| $\frac{ \tilde{u}_h }{akc} = A_u \left[1 - \beta_u \exp\left(-\left \frac{c}{U} - 1\right \right)\right] \exp(-\alpha_u kz)$ | 0.76 | 0.85 | 0.33 | | 0.64 |
| $\frac{ \tilde{w} }{akc} = A_w \left[1 - \beta_w \exp\left(-\left \frac{c}{U} - 1\right \right)\right] \exp(-\alpha_w kz)$ | 0.85 | 0.83 | 0.66 | | 0.76 |

when $c/U(z)$ is close to one, the measurements deviate from the function $F[c/U(z)]$, reaching a finite minimum while $F[c/U(z)]$ goes to zero. This deviation is not surprising since if the amplitude of the wave-induced fluctuations were to go to zero, the correlation between velocity fluctuations and wave elevation would also go to zero, and we would not have been able to sample them. Nevertheless, since we observed wave-induced fluctuations large enough to be detected when $c/U(z)$ is equal to one, it means that the proposed parameterization [Eq. (17)] is wrong and that a more realistic function needs to be used to better characterize the variations of the wave-induced velocities in the proximity of the critical layer. The divergence between the data and the current model is emphasized in Figs. 11c and 11d, where the bin-averaged data, plotted as a function of the normalized height, are scaled by the function $F[c/U(z)]$. In these panels, the data from the lowest levels (1 and 2) deviate from the best-fit functions $G(kz) = \exp(-\alpha kz)$ (orange lines) because, as we discussed before, wave-induced velocities measured at the lower levels are more subject to the effects of the critical layers than at higher levels. Therefore, the scaling by the function $F[c/U(z)]$, which underestimates the amplitude of the wave-induced velocities for data points where $c/U(z) \sim 1$, leads to an overcorrection of the wave age dependence when $c/U(z)$ is close to 1. This is clearly illustrated in Figs. 11c, 11d, and S2. These overcorrected points are responsible for large values of the bin-averaged data for both the horizontal and vertical components (see Figs. 11c,d).

To better parameterize the wave age dependence for small values of $c/U(z)$, we propose the following function F^* to account for the minimum values of the amplitude at $c/U(z) = 1$, using constants β and ζ :

$$F^*\left[\frac{c}{U(z)}\right] = 1 - \beta \exp\left[-\zeta \left|\frac{c}{U(z)} - 1\right|\right]. \quad (18)$$

The coefficient β defines the minimum values of the wave-induced velocity at the location of the critical layer, while the coefficient ζ adjusts how quickly the wave-induced fluctuations decrease approaching to the critical layer. The values of the coefficients for the best-fit functions minimizing the squared-difference cost function as well as the coefficients of determination are reported in Table 1. We want to stress that, if the coefficients β and ζ are set to one, the Taylor expansion of the function F^* at the first order is equivalent to the function F when $c/U(z)$ tends to one. Figure 12 shows the amplitude of the wave-induced velocities scaled by the functions $F^*[c/U(z)]$ and $G(kz)$ [Eqs. (18) and (16), respectively] as functions of $c/U(z)$ and kz . With this new parameterization, the collapse of the bin-averaged data from the five anemometers is excellent, each of them lying within the error bars of the other individual anemometer subsets of data. Raw data presented in Fig. S3 also show a reduced scatter of the data around the best-fit functions $F^*(c/U)$ and $G(kz)$. The vertical dependence with kz is similar to what was observed before with the previous scaling with the decay coefficient α_u equal to 0.85 for the horizontal velocity and $\alpha_w = 0.83$ for the vertical component. This result shows

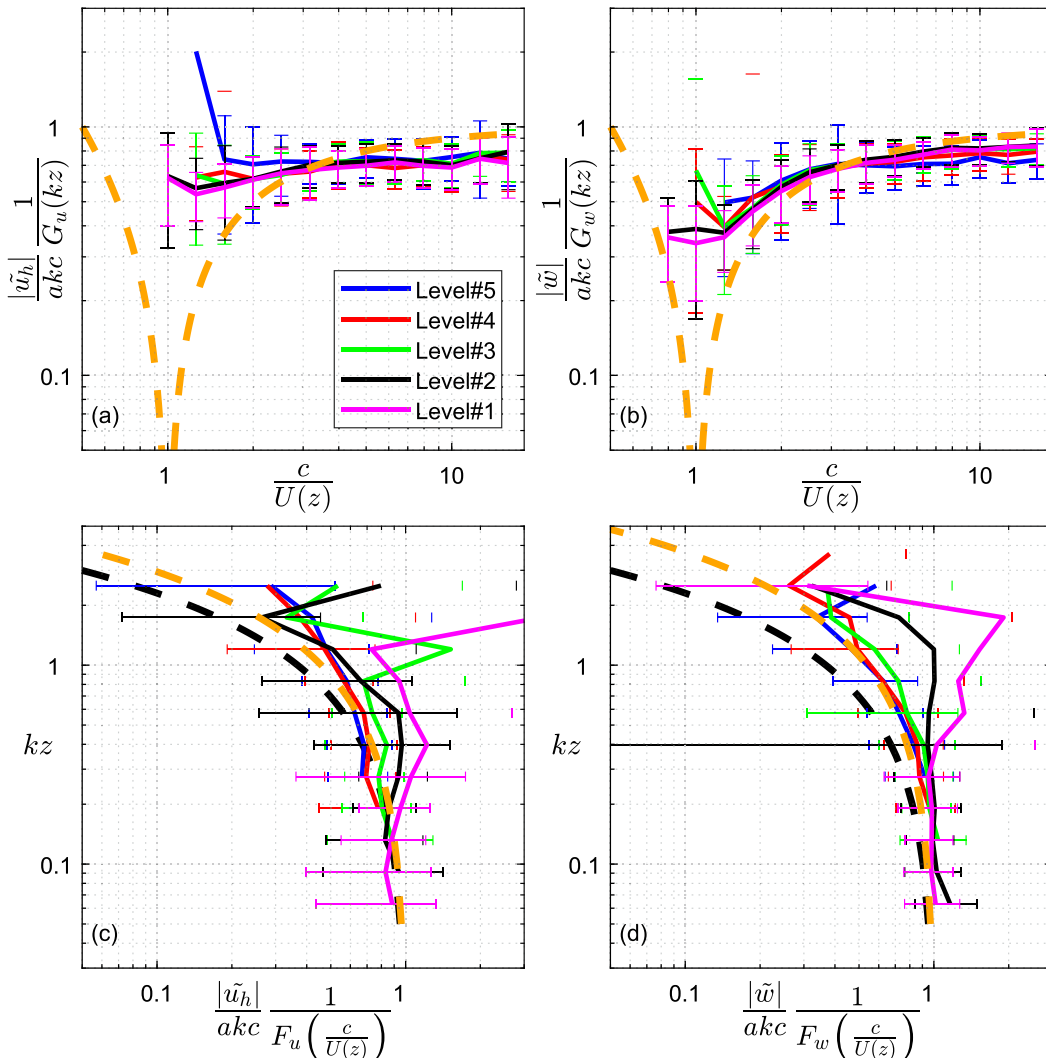


FIG. 11. The bin-averaged amplitude of the (left) horizontal and (right) vertical dimensionless wave-induced velocities (a),(b) corrected for their dependence on kz plotted as a function of the spectral wave age $c/U(z)$ and (c),(d) corrected for their dependence on $c/U(z)$ plotted as a function of the normalized height kz for each level. The functions $F[c/U(z)]$ in (a) and (b), $G_u(kz)$ in (c), and $G_w(kz)$ in (d) are plotted with dashed orange lines. Coefficients A_u and A_w are set to one, and the value of the coefficients α_u and α_w are reported in Table 1. The function $\exp(-kz)$ is plotted with dashed black lines in (c) and (d). Error bars correspond to the standard deviation of the data within each bin.

that both horizontal and vertical components follow the same exponential decay with kz . Values of α_i and A_i smaller than one means that the amplitude of the wave-induced velocities deviate from the exponential decay in $ack \exp(-kz)$ described by a potential airflow above waves forced at the surface by the orbital velocities ack . Several factors can explain this. The first obvious reason is that the presence of turbulence especially strong close to the surface can alter the decay rates of the wave-induced components through nonlinear interactions between the wave-induced and turbulent components of the airflow. Another reason can be due to the presence

of waves traveling in different directions, their resulting wave-induced components working against each other rather than adding up. Finally, the last reason would be the presence of current in the ocean responsible for a Doppler shift in the dispersion relationship. This creates a bias when converting frequencies into wavenumbers, therefore affecting both the vertical decay and the kinematic conditions at the surface, that is, A_i and α_i .

In Eq. (18), we introduced two degrees of freedom as F^* has two adjustable coefficients (β and ζ). It is remarkable that for both velocity components, the coefficient ζ is close to or equal to 1 ($\zeta_u = 0.96$ for the

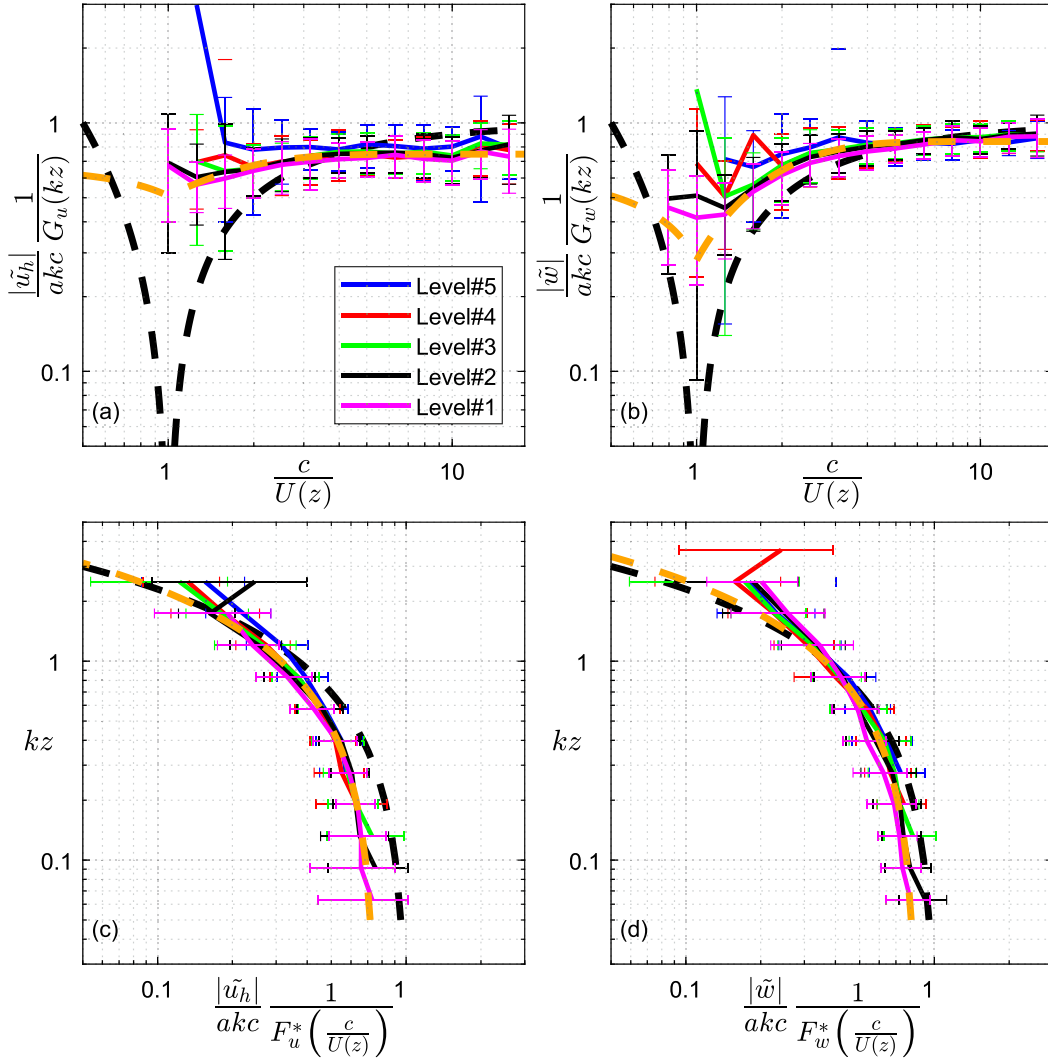


FIG. 12. The bin-averaged amplitude of the (left) horizontal and (right) vertical dimensionless wave-induced velocities (a),(b) corrected for their dependence on kz plotted as a function of the spectral wave age $c/U(z)$ and (c),(d) corrected for their dependence on $c/U(z)$ plotted as a function of the normalized height kz , for each level. The functions $A_u F_u^*[c/U(z)]$ in (a), $A_w F_w^*[c/U(z)]$ in (b), $A_u G_u(kz)$ in (c), and $A_w G_w(kz)$ in (d) are plotted with dashed orange lines. The coefficients of the functions above are all unconstrained, and their values are reported in Table 1. The functions $F(c/U) = |1 - U/c|$ in (a) and (b) and $\exp(-kz)$ in (c) and (d) are plotted with dashed black lines. Error bars correspond to the standard deviation of the data within each bin.

horizontal velocity and $\zeta_w = 1.00$ for the vertical velocity). By imposing $\zeta = 1$, the coefficients A , α , and β are equal (with less than $\pm 1\%$ – 2% difference) to those found when ζ is unconstrained. This implies that the wave age dependence can be parameterized with only one coefficient β to characterize the minimum value of the wave-induced amplitude at the critical height.

4. Discussion and conclusions

Field measurements of the airflow above ocean waves were conducted using a vertical array of ultrasonic

anemometers mounted on a telescopic mast attached to R/P *FLIP*. The spectral decomposition of the wind fluctuations led to the quantification of the amplitude and phase of the wave-induced fluctuations of the three components of the wind for frequencies ranging from 0.06 to 0.5 Hz. The telescopic mast permitted adjusting the height of the anemometers to adapt to environmental conditions, yielding measurements of the wind velocities from 2.6 m up to 15 m above the MSL. The range of heights covered by the array of anemometers coupled with the spectral decomposition of the wind fluctuations led to a description of the wave-induced

velocities at normalized heights kz ranging over more than one order of magnitude with values as low as $kz = 0.05$. Though the measurements were conducted over a wide range of wind and wave conditions, most of the wave-induced velocities we were able to measure were associated with spectral wave ages $c/U(z)$ greater than one, corresponding to measurements below the critical layers. Nevertheless, measurements in the neighborhood of the critical layers showed that the wave-induced velocities abruptly change phase across the critical layer and drop in amplitude. This corroborates the previous field observations from [Hristov et al. \(2003\)](#) and [Grare et al. \(2013a\)](#) and the theory of [Miles \(1957\)](#).

Measurements at several heights along with a proper normalization of the wave-induced velocities by the orbital velocity akc have highlighted their double dependence on both the spectral wave age $c/U(z)$ and the normalized height kz . We parameterized this double dependence using two independent functions $F[c/U(z)]$ and $G(kz)$. Our results show that below the influence of the critical layer, the wave-induced velocities decay with normalized height following an exponential curve $\exp(-\alpha kz)$, where α is a constant equal to 0.84 ± 0.01 for both the horizontal and the vertical velocities.

Our results are consistent with the early work from [Kitaigorodskii et al. \(1983\)](#) with data collected on Lake Ontario over a small range of wave ages ($C_p/U_{10} \leq 1$), focusing only on the exponential decay with height of the wave-induced velocities. Recent LES results from [Wu et al. \(2017\)](#) for wind-following swell conditions also show an exponential decay of the wave-induced velocities. Data presented in [Fig. 1](#) of their publication correspond to wave ages $C_p/U_{10} = 2.5$ and 4.3 , with waves of 100-m length and at altitudes up to 30 m. At these wave ages, data presented were well below the critical layer, therefore away from its influence. They found a decay coefficient for the streamwise component ranging from 0.85 to 0.93 (they present nonnormalized decay coefficients of the variance of the wave-induced velocities ranging from 0.107 to 0.117 for 100-m-long waves). For the vertical component, they found a decay coefficient slightly higher in the range of 1.04–1.12, consistent with our experimental measurements.

We showed that the dependence on the wave age c/U can simply be parameterized by the function $F^*(c/U) = 1 - \beta \exp[(c/U) - 1]$. The term $\exp[(c/U) - 1]$ accounts for the decrease of the amplitude of the wave-induced velocity across the critical layer, while the coefficient β parameterizes the minimum value reached by these velocities when c/U is equal to 1 (i.e., exactly at the critical height). [Soloviev and Kudryavtsev \(2010\)](#)

have studied the vertical profile of the wave-induced streamwise component of the wind above swell both in following-wind swell and opposite-swell wind conditions. They showed that these profiles follow an exponential decay $\exp(-k_p z)$, where k_p is the peak wavenumber of the swell, and that they also depend on the inverse wave age weighted for the angle difference between the swell direction and the wind direction. They show a slight difference between following-wind swell and opposing-wind swell; the latter case producing swell-induced fluctuations slightly more intense than the first case. As their study focuses on the effect of swell on the airflow, their measurements were performed below the critical height, that is, for $c/U > 1$, meaning that the effect of the critical layer is likely to be minimal in their study. This is consistent with our findings, which show that away from the critical layers, the spectral wave age dependence can be simply parameterized using the function $F(c/U) = |1 - U/c|$. Their approach is different from ours, since the amplitude of the wave-induced fluctuations was computed in their study using narrow-banded frequency-averaged values around the peak of the swell, while our approach resolves any coherent fluctuations at any frequency regardless of the wave type (i.e., swell or wind waves). Another difference is the way the angle between the waves and the wind is taken into account. [Soloviev and Kudryavtsev \(2010\)](#) compute the mean direction of the swell (which is well separated in both direction and frequency from the rest of the wave field, e.g., wind waves), and they scale their results using the inverse wave age $(U \cos \beta)/c_p$, where β is the angle between the wind and the swell directions. In our paper, the angle between the wind and wave directions is handled differently because of the complexity of the wave field experienced during the experiment with a superposition of swells from different directions in the same range of frequencies (see [Figs. 5 and 6](#)). To circumvent this difficulty, instead of focusing only on the streamwise (relative to the mean wind direction) wave-induced velocity \tilde{u} , we computed the omnidirectional amplitude of the horizontal wave-induced velocity $|\tilde{u}_h| = \sqrt{|\tilde{u}|^2 + |\tilde{v}|^2}$, where \tilde{v} is the crosswind wave-induced velocity. This technique is simple to implement and accounts for all the directional components of the wave field. However, with this technique, we introduce two assumptions.

First, it is assumed that, at a given frequency, all the waves have the same wave age; in other words, the wind forcing (i.e., the inverse wave age) is the same regardless of the angle between the wind and the wave directions. However, the formulation of the inverse wave age accounting for the misalignment between the wind and the

waves is a still controversial topic (Hanley et al. 2010; Hogstrom et al. 2011; Hanley et al. 2011), and further discussion of this subject is beyond the scope of this paper.

Second, for a case where two or more wave fields with the same dominant phase speed c are traveling in different directions, it is assumed that their corresponding horizontal wave-induced velocities do not interact with each other and that the amplitude of the horizontal wave-induced fluctuations coherent with the phase of these wave fields is linearly related to the vertical displacement of the surface resulting from the superposition of these wave fields.

Regarding the two points above, we emphasize that for most of the experiment, the waves were mostly aligned with the wind and that when it was not the case, for example, when a south swell was superposed upon the northwest wind and waves, the wave energy associated with the south swell accounted for less than 20% of the total wave energy. Therefore, we believe that using a spectral wave age that does not account for the misalignment between the wind and the waves, and presenting data in the form of $|\bar{u}_h|$, is acceptable for this work.

Acknowledgments. We thank Tom Golfinos and the crew of the R/P *FLIP* for their tireless support of this research and Captain Bill Gaines for his logistical support of *FLIP* operations. The measurements would not have been possible without the work of Peter Sutherland, Luc Deike, and Nick Statom during the experiment. The manuscript also benefited from the helpful suggestions of two anonymous reviewers. This research was supported by funding to WKM from the physical oceanography programs at ONR (Grants N00014-14-1-0710 and N00014-12-1-1022) and NSF (Grants OCE-1634289 and OCE-1155403).

REFERENCES

- Al-Zanaidi, M. A., and W. H. Hui, 1984: Turbulent airflow over water waves—A numerical study. *J. Fluid Mech.*, **148**, 225–246, <https://doi.org/10.1017/S0022112084002329>.
- Banner, M. L., and W. L. Peirson, 1998: Tangential stress beneath wind-driven air–water interfaces. *J. Fluid Mech.*, **364**, 115–145, <https://doi.org/10.1017/S0022112098001128>.
- Belcher, S. E., and J. C. R. Hunt, 1993: Turbulent shear flow over slowly moving waves. *J. Fluid Mech.*, **251**, 109–148, <https://doi.org/10.1017/S0022112093003350>.
- Bendat, J. S., and A. G. Piersol, 2010: *Random Data Analysis and Measurement Procedures*. 4th ed. Wiley and Sons, 640 pp.
- Buckley, M. P., and F. Veron, 2016: Structure of the airflow above surface waves. *J. Phys. Oceanogr.*, **46**, 1377–1397, <https://doi.org/10.1175/JPO-D-15-0135.1>.
- Dobson, F. W., 1971: Measurements of atmospheric pressure on wind-generated sea waves. *J. Fluid Mech.*, **48**, 91–127, <https://doi.org/10.1017/S0022112071001496>.
- Donelan, M. A., A. V. Babanin, I. R. Young, and M. L. Banner, 2006: Wave-follower field measurements of the wind-input spectral function. Part II: Parameterization of the wind input. *J. Phys. Oceanogr.*, **36**, 1672–1689, <https://doi.org/10.1175/JPO2933.1>.
- Edson, J. B., A. A. Hinton, K. E. Prada, J. E. Hare, and C. W. Fairall, 1998: Direct covariance flux estimates from mobile platforms at sea. *J. Atmos. Oceanic Technol.*, **15**, 547–562, [https://doi.org/10.1175/1520-0426\(1998\)015<0547:DCFEFM>2.0.CO;2](https://doi.org/10.1175/1520-0426(1998)015<0547:DCFEFM>2.0.CO;2).
- Elliott, J. A., 1972: Microscale pressure fluctuations near waves being generated by the wind. *J. Fluid Mech.*, **54**, 427–448, <https://doi.org/10.1017/S0022112072000783>.
- Gent, P. R., and P. A. Taylor, 1976: A numerical model of the air flow above water waves. *J. Fluid Mech.*, **77**, 105–128, <https://doi.org/10.1017/S0022112076001158>.
- Grare, L., L. Lenain, and W. K. Melville, 2013a: Wave-coherent airflow and critical layers over ocean waves. *J. Phys. Oceanogr.*, **43**, 2156–2172, <https://doi.org/10.1175/JPO-D-13-056.1>.
- , W. L. Peirson, H. Branger, J. W. Walker, J.-P. Giovanangeli, and V. Makin, 2013b: Growth and dissipation of wind-forced, deep-water waves. *J. Fluid Mech.*, **722**, 5–50, <https://doi.org/10.1017/jfm.2013.88>.
- , L. Lenain, and W. K. Melville, 2016: The influence of wind direction on Campbell scientific CSAT3 and Gill R3-50 sonic anemometer measurements. *J. Atmos. Oceanic Technol.*, **33**, 2477–2497, <https://doi.org/10.1175/JTECH-D-16-0055.1>.
- Hanley, K. E., S. E. Belcher, and P. P. Sullivan, 2010: A global climatology of wind–wave interaction. *J. Phys. Oceanogr.*, **40**, 1263–1282, <https://doi.org/10.1175/2010JPO4377.1>.
- , —, and —, 2011: Reply. *J. Phys. Oceanogr.*, **41**, 1814–1817, <https://doi.org/10.1175/JPO-D-11-051.1>.
- Hanson, J. L., and O. M. Phillips, 2001: Automated analysis of ocean surface directional wave spectra. *J. Atmos. Oceanic Technol.*, **18**, 277–293, [https://doi.org/10.1175/1520-0426\(2001\)018<0277:AAOOSD>2.0.CO;2](https://doi.org/10.1175/1520-0426(2001)018<0277:AAOOSD>2.0.CO;2).
- Hare, J. E., T. Hara, J. B. Edson, and J. M. Wilczak, 1997: A similarity analysis of the structure of airflow over surface waves. *J. Phys. Oceanogr.*, **27**, 1018–1037, [https://doi.org/10.1175/1520-0485\(1997\)027<1018:ASAOTS>2.0.CO;2](https://doi.org/10.1175/1520-0485(1997)027<1018:ASAOTS>2.0.CO;2).
- Hogstrom, U., A. Smedman, E. Sahlee, W. M. Drennan, K. K. Kahma, H. Pettersson, and F. Zhang, 2009: The atmospheric boundary layer during swell: A field study and interpretation of the turbulent kinetic energy budget for high wave ages. *J. Atmos. Sci.*, **66**, 2764–2779, <https://doi.org/10.1175/2009JAS2973.1>.
- , —, A. Semedo, and A. Rutgersson, 2011: Comments on “A global climatology of wind–wave interaction.” *J. Phys. Oceanogr.*, **41**, 1811–1813, <https://doi.org/10.1175/JPO-D-10-05015.1>.
- , E. Sahlee, A.-S. Smedman, A. Rutgersson, E. Nilsson, K. K. Kahma, and W. M. Drennan, 2015: Surface stress over the ocean in swell-dominated conditions during moderate winds. *J. Atmos. Sci.*, **72**, 4777–4795, <https://doi.org/10.1175/JAS-D-15-0139.1>.
- Hristov, T., and J. Ruiz-Plancarte, 2014: Dynamic balances in a wavy boundary layer. *J. Phys. Oceanogr.*, **44**, 3185–3194, <https://doi.org/10.1175/JPO-D-13-0209.1>.
- , S. D. Miller, and C. A. Friehe, 2003: Dynamical coupling of wind and ocean waves through wave-induced air flow. *Nature*, **422**, 55–58, <https://doi.org/10.1038/nature01382>.
- Hsu, C.-T., and E. Y. Hsu, 1983: On the structure of turbulent flow over a progressive water wave: Theory and experiment in a transformed wave-following coordinate system. Part 2. *J. Fluid Mech.*, **131**, 123–153, <https://doi.org/10.1017/S0022112083001263>.
- Hussain, A. K. M. F., and W. C. Reynolds, 1970: The mechanics of an organized wave in turbulent shear flow. *J. Fluid Mech.*, **41**, 241–258, <https://doi.org/10.1017/S0022112070000605>.

- Jacobs, S. J., 1987: An asymptotic theory for the turbulent flow over a progressive water wave. *J. Fluid Mech.*, **174**, 69–80, <https://doi.org/10.1017/S0022112087000041>.
- Janssen, P. A. E. M., 1991: Quasi-linear theory of wind-wave generation applied to wave forecasting. *J. Phys. Oceanogr.*, **21**, 1631–1642, [https://doi.org/10.1175/1520-0485\(1991\)021<1631:QLTOWW>2.0.CO;2](https://doi.org/10.1175/1520-0485(1991)021<1631:QLTOWW>2.0.CO;2).
- Jeffreys, H., 1925: On the formation of water waves by wind. *Proc. Roy. Soc. London*, **107A**, 189–206, <https://doi.org/10.1098/rspa.1925.0015>.
- Kihara, N., H. Hanazaki, T. Mizuya, and H. Ueda, 2007: Relationship between airflow at the critical height and momentum transfer to the traveling waves. *Phys. Fluids*, **19**, 015102, <https://doi.org/10.1063/1.2409736>.
- Kitaigorodskii, S. A., M. A. Donelan, J. L. Lumley, and E. A. Terray, 1983: Wave–turbulence interactions in the upper ocean. Part II: Statistical characteristics of wave and turbulent components of the random velocity field in the marine surface layer. *J. Phys. Oceanogr.*, **13**, 1988–1999, [https://doi.org/10.1175/1520-0485\(1983\)013<1988:WTIITU>2.0.CO;2](https://doi.org/10.1175/1520-0485(1983)013<1988:WTIITU>2.0.CO;2).
- Kudryavtsev, V. N., and V. K. Makin, 2004: Impact of swell on the marine atmospheric boundary layer. *J. Phys. Oceanogr.*, **34**, 934–949, [https://doi.org/10.1175/1520-0485\(2004\)034<0934:IOSOTM>2.0.CO;2](https://doi.org/10.1175/1520-0485(2004)034<0934:IOSOTM>2.0.CO;2).
- , —, and J. F. Meirink, 2001: Simplified model of the air flow above waves. *Bound.-Layer Meteor.*, **100**, 63–90, <https://doi.org/10.1023/A:1018914113697>.
- Lighthill, M. J., 1957: The fundamental solution for small steady three-dimensional disturbances to a two-dimensional parallel shear flow. *J. Fluid Mech.*, **3**, 113–144, <https://doi.org/10.1017/S002211205700052X>.
- , 1962: Physical interpretation of the mathematical theory of wave generation by wind. *J. Fluid Mech.*, **14**, 385–398, <https://doi.org/10.1017/S0022112062001305>.
- Liu, Y., D. Yang, X. Guo, and L. Shen, 2010: Numerical study of pressure forcing of wind on dynamically evolving water waves. *Phys. Fluids*, **22**, 041704, <https://doi.org/10.1063/1.3414832>.
- Mastenbroek, C., V. K. Makin, M. H. Garat, and J. P. Giovanangeli, 1996: Experimental evidence of the rapid distortion of turbulence in the air flow over water waves. *J. Fluid Mech.*, **318**, 273–302, <https://doi.org/10.1017/S0022112096007124>.
- Miles, J. W., 1957: On the generation of surface waves by shear flows. *J. Fluid Mech.*, **3**, 185–204, <https://doi.org/10.1017/S0022112057000567>.
- , 1993: Surface-wave generation revisited. *J. Fluid Mech.*, **256**, 427–441, <https://doi.org/10.1017/S0022112093002836>.
- Monin, A., and A. Obukhov, 1954: Basic laws of turbulent mixing in the surface layer of the atmosphere. *Tr. Geofiz. Inst., Akad. Nauk SSSR*, **24**, 163–187.
- Phillips, O. M., 1957: On the generation of waves by turbulent wind. *J. Fluid Mech.*, **2**, 417–445, <https://doi.org/10.1017/S0022112057000233>.
- Plant, W. J., 1982: A relationship between wind stress and wave slope. *J. Geophys. Res.*, **87**, 1961–1967, <https://doi.org/10.1029/JC087iC03p01961>.
- Portilla, J., F. J. Ocampo-Torres, and J. Monbaliu, 2009: Spectral partitioning and identification of wind sea and swell. *J. Atmos. Oceanic Technol.*, **26**, 107–122, <https://doi.org/10.1175/2008JTECHO609.1>.
- Smedman, A., U. Hogstrom, E. Sahlée, W. M. Drennan, K. K. Kahma, H. Pettersson, and F. Zhang, 2009: Observational study of marine atmospheric boundary layer characteristics during swell. *J. Atmos. Sci.*, **66**, 2747–2763, <https://doi.org/10.1175/2009JAS2952.1>.
- Smith, J. A., and K. F. Rieder, 1997: Wave induced motion of FLIP. *Ocean Eng.*, **24**, 95–110, [https://doi.org/10.1016/0029-8018\(96\)00008-X](https://doi.org/10.1016/0029-8018(96)00008-X).
- Snyder, R. L., F. W. Dobson, J. A. Elliott, and R. B. Long, 1981: Array measurements of atmospheric pressure fluctuations above surface gravity waves. *J. Fluid Mech.*, **102**, 1–59, <https://doi.org/10.1017/S0022112081002528>.
- Soloviev, Y. P., and V. N. Kudryavtsev, 2010: Wind-speed undulations over swell: Field experiment and interpretation. *Bound.-Layer Meteor.*, **136**, 341–363, <https://doi.org/10.1007/s10546-010-9506-z>.
- Sullivan, P. P., J. C. McWilliams, and C.-H. Moeng, 2000: Simulation of turbulent flow over idealized water waves. *J. Fluid Mech.*, **404**, 47–85, <https://doi.org/10.1017/S0022112099006965>.
- , J. B. Edson, T. Hristov, and J. C. McWilliams, 2008: Large-eddy simulations and observations of atmospheric marine boundary layers above nonequilibrium surface waves. *J. Atmos. Sci.*, **65**, 1225–1245, <https://doi.org/10.1175/2007JAS2427.1>.
- , J. C. McWilliams, and E. G. Patton, 2014: Large-eddy simulation of marine atmospheric boundary layers above a spectrum of moving waves. *J. Atmos. Sci.*, **71**, 4001–4027, <https://doi.org/10.1175/JAS-D-14-0095.1>.
- Townsend, A. A., 1972: Flow in a deep turbulent boundary layer over a surface distorted by water waves. *J. Fluid Mech.*, **55**, 719–735, <https://doi.org/10.1017/S0022112072002101>.
- Van Duin, C. A., and P. A. E. M. Janssen, 1992: An analytic model of the generation of surface gravity waves by turbulent air flow. *J. Fluid Mech.*, **236**, 197–215, <https://doi.org/10.1017/S0022112092001393>.
- Veron, F., G. Saxena, and S. K. Misra, 2007: Measurements of the viscous tangential stress in the airflow above wind waves. *Geophys. Res. Lett.*, **34**, L19603, <https://doi.org/10.1029/2007GL031242>.
- , W. K. Melville, and L. Lenain, 2008: Wave-coherent air–sea heat flux. *J. Phys. Oceanogr.*, **38**, 788–802, <https://doi.org/10.1175/2007JPO3682.1>.
- , —, and —, 2009: Measurements of ocean surface turbulence and wave–turbulence interactions. *J. Phys. Oceanogr.*, **39**, 2310–2323, <https://doi.org/10.1175/2009JPO4019.1>.
- WAFO Group, 2000: WAFO. Department of Mathematical Statistics, Centre for Mathematical Sciences, Lund University, <http://www.maths.lth.se/matstat/wafo/>.
- Wilczak, J., S. Oncley, and S. Stage, 2001: Sonic anemometer tilt correction algorithms. *Bound.-Layer Meteor.*, **99**, 127–150, <https://doi.org/10.1023/A:1018966204465>.
- Wu, L., A. Rutgersson, and E. Nilsson, 2017: Atmospheric boundary layer turbulence closure scheme for wind-following swell conditions. *J. Atmos. Sci.*, **74**, 2363–2382, <https://doi.org/10.1175/JAS-D-16-0308.1>.
- , T. Hristov, and A. Rutgersson, 2018: Vertical profiles of wave-coherent momentum flux and velocity variances in the marine atmospheric boundary layer. *J. Phys. Oceanogr.*, **48**, 625–641, <https://doi.org/10.1175/JPO-D-17-0052.1>.
- Yang, D., and L. Shen, 2009: Characteristics of coherent vortical structures in turbulent flows over progressive surface waves. *Phys. Fluids*, **21**, 125106, <https://doi.org/10.1063/1.3275851>.
- , and —, 2010: Direct-simulation-based study of turbulent flow over various waving boundaries. *J. Fluid Mech.*, **650**, 131–180, <https://doi.org/10.1017/S0022112009993557>.
- , C. Meneveau, and L. Shen, 2013: Dynamic modelling of sea-surface roughness for large-eddy simulation of wind over ocean wavefield. *J. Fluid Mech.*, **726**, 62–99, <https://doi.org/10.1017/jfm.2013.215>.
- Young, W. R., and C. L. Wolfe, 2014: Generation of surface waves by shear-flow instability. *J. Fluid Mech.*, **739**, 276–307, <https://doi.org/10.1017/jfm.2013.617>.